gels

MDPI

Review

A Beginner's Guide to the Characterization of Hydrogel Microarchitecture for Cellular Applications

Francisco Drusso Martinez-Garcia [1,2], Tony Fischer [3], Alexander Hayn [3,4], Claudia Tanja Mierke [3,*], Janette Kay Burgess [1,2,5] and Martin Conrad Harmsen [1,2,5,*]

1 Department of Pathology and Medical Biology, University Medical Center Groningen, University of Groningen, Hanzeplein 1 (EA11), 9713 GZ Groningen, The Netherlands
2 W.J. Kolff Research Institute, University Medical Center Groningen, University of Groningen, A. Deusinglaan 1, 9713 AV Groningen, The Netherlands
3 Biological Physics Division, Peter Debye Institute of Soft Matter Physics, Faculty of Physics and Earth Science, Leipzig University, Linnéstraße 5, 04103 Leipzig, Germany
4 Clinic and Polyclinic for Oncology, Gastroenterology, Hepatology, Pneumology, Infectiology Department of Hepatology, University Hospital Leipzig, Liebigstr. 19, 04103 Leipzig, Germany
5 Groningen Research Institute for Asthma and COPD (GRIAC), University Medical Center Groningen, University of Groningen, Hanzeplein 1 (EA11), 9713 AV Groningen, The Netherlands
* Correspondence: claudia.mierke@uni-leipzig.de (C.T.M.); m.c.harmsen@umcg.nl (M.C.H.)

Abstract: The extracellular matrix (ECM) is a three-dimensional, acellular scaffold of living tissues. Incorporating the ECM into cell culture models is a goal of cell biology studies and requires biocompatible materials that can mimic the ECM. Among such materials are hydrogels: polymeric networks that derive most of their mass from water. With the tuning of their properties, these polymer networks can resemble living tissues. The microarchitectural properties of hydrogels, such as porosity, pore size, fiber length, and surface topology can determine cell plasticity. The adequate characterization of these parameters requires reliable and reproducible methods. However, most methods were historically standardized using other biological specimens, such as 2D cell cultures, biopsies, or even animal models. Therefore, their translation comes with technical limitations when applied to hydrogel-based cell culture systems. In our current work, we have reviewed the most common techniques employed in the characterization of hydrogel microarchitectures. Our review provides a concise description of the underlying principles of each method and summarizes the collective data obtained from cell-free and cell-loaded hydrogels. The advantages and limitations of each technique are discussed, and comparisons are made. The information presented in our current work will be of interest to researchers who employ hydrogels as platforms for cell culture, 3D bioprinting, and other fields within hydrogel-based research.

Keywords: extracellular matrix; hydrogel architecture; topography; porosity; electron microscopy; laser microscopy; micro-computed tomography; second harmonic generation; atomic force microscopy

Citation: Martinez-Garcia, F.D.; Fischer, T.; Hayn, A.; Mierke, C.T.; Burgess, J.K.; Harmsen, M.C. A Beginner's Guide to the Characterization of Hydrogel Microarchitecture for Cellular Applications. *Gels* **2022**, *8*, 535. https://doi.org/10.3390/gels8090535

Academic Editors: Esmaiel Jabbari, Lucília P. da Silva, Alexandra P. Marques and Rui L. Reis

Received: 30 June 2022
Accepted: 23 August 2022
Published: 26 August 2022

1. Introduction

The ECM is a three-dimensional (3D), acellular, heterogeneous network composed of fibrillar force-transducing collagens, interconnecting proteins such as fibronectin, matricellular proteins (e.g., periostin, fibulins, osteopontin), and the basement membrane proteins collagen type-IV and laminin [1]. Water retention is accomplished primarily by the highly negatively charged glycosaminoglycans (GAGs) or their higher order structures, i.e., GAGs bound to a protein core (proteoglycans), and to a lesser extent by collagens and similar proteins that also retain water [2]. The water concentration is highly tissue-specific, but it can range from 5% to 90% [3]. The ECM provides structural support and instruction to cells governed by its biophysical and biochemical cues.

Among the materials employed to mimic the ECM are hydrogels: highly porous, interconnected, hydrophilic, 3D polymeric networks that absorb and hold over 20% of their

mass in water or other biological fluids [4,5]. When loaded with cells, hydrogels can provide biophysical conditions similar to those found in the native ECM [6,7]. For example, cell adhesion is not limited to a single plane, and there is no forced polarity as observed in vivo. Instead, in hydrogels, cell spreading and migration are modulated due to the variable stiffness and viscoelasticity of the material [8,9]. Hydrogels are formed via physical and chemical crosslinks and are commonly classified based on their polymer sources [4,10,11]. Fibrin [12], collagen [13], and decellularized organ-derived ECM [14–18] are examples of natural hydrogels and are regarded as biocompatible and bioactive [19]. These materials retain native cell-binding sites as well as protease-targeted degradation motifs, but due to their sources, batch-to-batch variations can influence the hydrogels' tunability and overall mechanics and microarchitecture [10,19,20]. Synthetic hydrogels, such as polyacrylamide and polyethylene glycol (PEG), are regarded as more tunable than natural hydrogels, as their reconstitution conditions result in fewer batch-to-batch variations. Modifying the polymer backbones and molecular weights of synthetic hydrogels are common approaches to fine-tuning their properties. However, synthetic hydrogels lack inherent fundamental biological cues and require conjugation with cell-binding peptides (e.g., RGD, GFOGER, and IKVAV) to be biocompatible [10,21–23]. Semi-synthetic hydrogels, such as gelatin methacryloyl (GelMA) [24–27] or methacrylated hyaluronic acid (HAMA) [28,29], stem from the incorporation of crosslinking sites into the backbone of a natural polymer. These sites grant semi-synthetic hydrogels with a mechanical stability and tunability not commonly achieved in natural hydrogels [30–32]. Semi-synthetic hydrogels retain some biocompatible and bioactive features, being derivatives of natural polymers. For a more detailed description of the properties of individual hydrogel polymers, the reader is referred elsewhere [4,19,33]. The wide variety of polymers available for cell culture assays allow researchers to tailor hydrogel-based cell culture models to their research question(s). Within hydrogels, the microarchitecture is an inherent property known to influence the cell fate [34–36].

Hydrogel Microarchitecture

In biology, microarchitecture refers to the detailed structure of any organ at a micrometer scale. In hydrogels, the microarchitecture depends on the organization of the polymer network during the sol–gel transition, the polymer concentration, and the crosslinking conditions (e.g., ionic strength, temperature, and pH), among others [37,38]. The resulting polymer network, known as the mesh size or molecular porosity, influences oxygen and nutrient diffusion [39]. Porosity is the percentage of void space in a material and it represents a fraction of the total volume [40,41]. Pore sizes influence contact guidance during cell migration or inhibit cell orientation [42,43]. A lower porosity induces cell aggregation and inhibits proliferation (e.g., 93% vs. 97% porosity) [44]. Large-sized pores may compromise the mechanical stability of the polymer network due to the excessive void, depending on the crosslinks holding the network together [45,46]. In hydrogel-based tissue engineering, pore size is critical for bone (>300 μm) [40,47], (250–500 μm) cartilage [48], and vascular network formation (~166 μm) [49] to occur both in vivo [40,50–52] and in vitro [40,47,53]. Nonetheless, such processes are not solely pore size-dependent [45], highlighting the importance of ECM composition [45] and conformation [37] in determining the cell fate. Other components of hydrogel microarchitectures include the fiber diameter, length, and orientation [42,54–56], as well as network inhomogeneity [57], which play an active role in cell invasion [58–62]. For example, in a cancer cell model, the cell morphology, cluster formation, and cell invasion were regulated by the fiber diameter (850 nm) and not the pore size (7.5–11 μm) [58].

Cell–matrix interactions can change the hydrogel microarchitecture, with diverse outcomes based on the polymer type [63,64]. Additional microarchitecture parameters, such as surface topography, are mostly described in 2D hydrogel-based cell culture models. Topographic stimuli also influence cell adhesion [65], contact guidance [66,67], migration [65], and overall gene regulation [66,68,69].

Due to its relevance in hydrogel-based research, microarchitecture is of increasing interest to researchers, and the number of publications has substantially grown over the years (Figure 1). The data reported on hydrogel microarchitecture depend on the method employed to assess it, and the systematic errors behind said method need to be carefully considered. Therefore, the present work aims to provide an overview of how those data are produced. Our study's novel aim is to integrate the known techniques and facilitate the choice of methods by relatively inexperienced investigators in order to improve understandings of 'cells in gels' in this multidisciplinary field. Thee accurate rate quantification of the microarchitectural parameters in biopolymer networks is essential for elucidating the observed effects of hydrogels on cell biology. Most methods used for assessing hydrogel microarchitecture can be classified as electron-based or photon-based, based on their underlying principles, and they are further explained in this work.

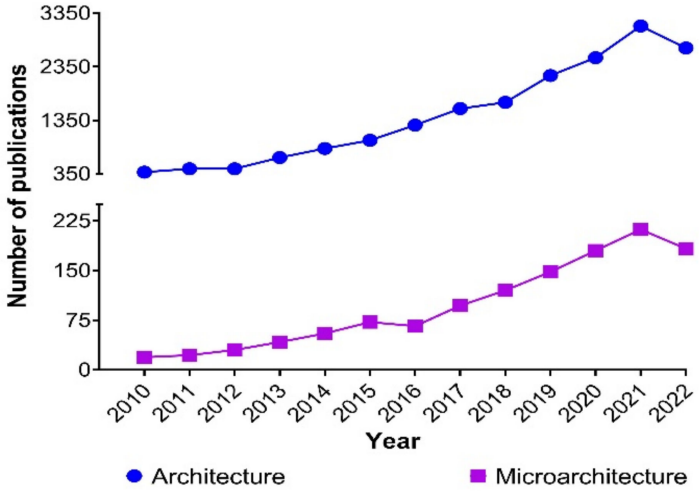

Figure 1. Publications per year from 2010 to June 2022 in the SCOPUS® database (accessed on 21 June 2022), including review articles, research articles, book chapters, conference abstracts, book reviews, conference papers, editorials, mini-reviews, and short communications in all areas of knowledge, using the keywords "hydrogel architecture" (n = 18,751) and "hydrogel microarchitecture" (n = 1246).

2. Electron-Based Techniques

2.1. Scanning Electron Microscopy

Scanning electron microscopy (SEM) is the most widely reported method for characterizing hydrogel microarchitectures [17,20,38,63,70–77]. This high-resolution imaging tool provides a detailed visualization of the hydrogel surface at the nanometer scale [78]. As its name suggests, SEM is an electron-based technique, where a high energy beam (aka "electron gun") bombards a metal- or carbon-coated specimen with primary electrons, causing the emission of secondary and backscattered electrons. Secondary electrons highlight the morphology and topography of the specimen, while backscattered electrons provide contrast between areas with distinct chemical compositions (Figure 2). SEM imaging occurs under a high vacuum, as the presence of gas can attenuate the electron beams and stop them from scattering [79]. SEM microphotographs of hydrogels are employed to determine pore size, pore distribution, and porosity percentage, as well as fiber thickness and fiber orientation [17,38,63,72–74]. In cell-loaded hydrogels, the visualization of the cells is also possible [80–84]. The analytical capabilities of SEM include X-ray-based tools, such as energy dispersive X-Ray spectroscopy (EDX). EDX can detect elements such as C, S, O, N, Na, and others that are present in hydrogels [85–88] and within cells (e.g., P—a marker of DNA) (Figure 3A). EDX is particularly useful for the recognition of cells present within hydrogels of marked structural heterogeneity (Figure 3B). For more in-depth information on the use of EDX in biomedical research and diagnosis, the reader is referred elsewhere [89].

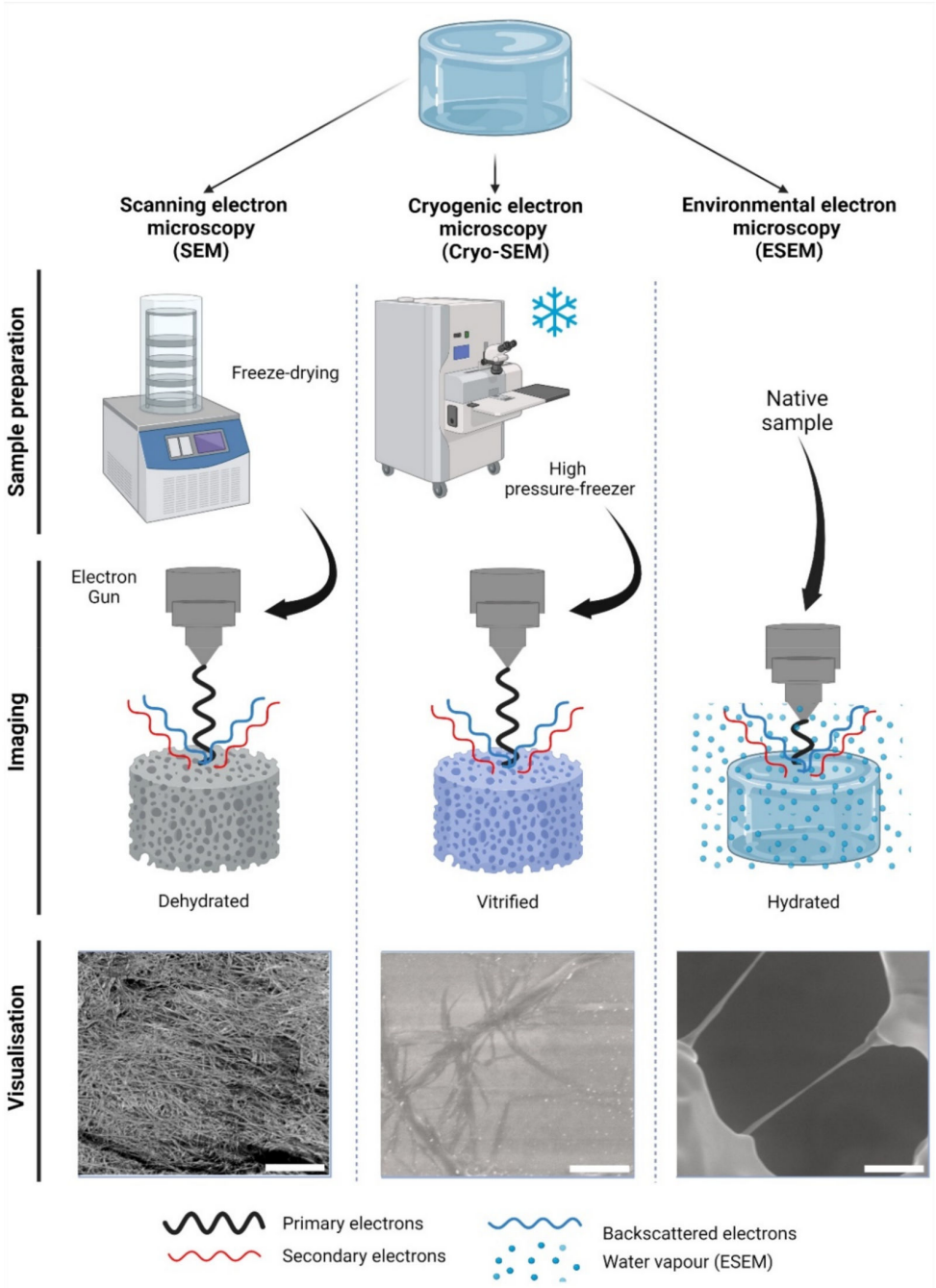

Figure 2. Electron-based imaging techniques for hydrogels. Standard scanning electron microscopy (SEM) relies on sample dehydration, including freeze-drying (shown) after fixation with aldehydes, followed by metal coating. Due to dehydration, the network appears condensed in visualization. In cryogenic SEM (Cryo-SEM), samples are vitrified using—among other methods—a high-pressure freezer (shown). Solid water ice is a source of imaging errors and is seen during imaging. In contrast, environmental SEM (ESEM) does not require a particular sample preparation, as it remains hydrated within a humidified chamber. In ESEM, the electron gun is closer to the specimen than in SEM or Cryo-SEM during imaging. As shown, single collagen fibers can be visualized; however, water condensation can cause imaging artefacts. The visualization of collagen type-I hydrogels (3.0 g/L) is shown at 12,000× magnification, 5 kV, and z = 9 mm. Scale bars represent 5 µm. Collagen type I hydrogels preparation, SEM, Cryo-SEM and ESEM detailed in Appendix A.

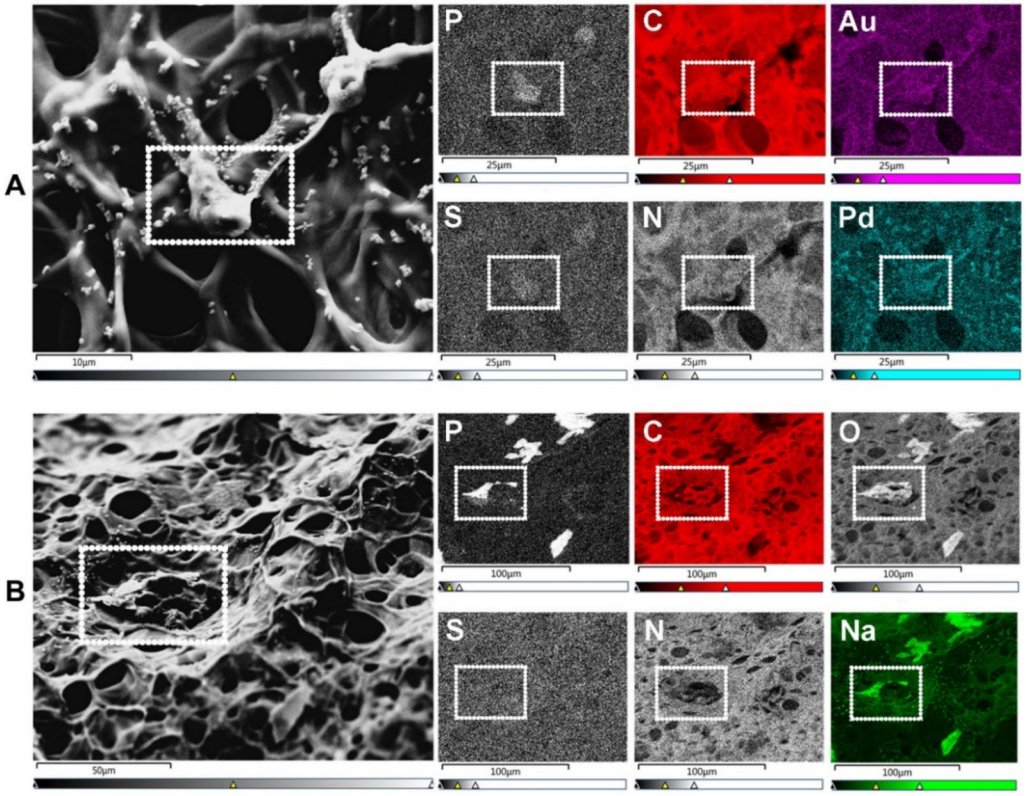

Figure 3. SEM-energy dispersive X-ray spectroscopy (EDX) elemental mapping. Images show human umbilical vein endothelial cells (HUVECs) on the surface of a gelatin methacryloyl (GelMA) hydrogel. (**A**) SEM allows for the visualization of cells (surrounded by a white dotted rectangle), while EDX identifies the elements present in both cells and hydrogels. These elements include non-metals such as phosphorus (P—a marker of DNA/nuclei), carbon (C), sulfur (S), and nitrogen (N). Transition metals used for coatings, such as gold (Au) and palladium (Pd), are also identified with EDX. Scale bars represent 10 μm and 25 μm. (**B**) In specimens with marked heterogeneity, EDX facilitates the identification of cells on the hydrogel surface (white dotted rectangle) that otherwise would not be distinguishable due to the condensation of the polymer network. Additional elements relevant to cell biology include non-metals, e.g., oxygen (O), and alkali metals, e.g., sodium (Na). Scale bars represent 50 μm and 100 μm. HUVEC's culture conditions and GelMA properties detailed in Appendix A.

SEM-generated data indicate that higher polymer concentrations decrease pore sizes, but that cells are capable of modifying such porosity in hydrogels with degradation-sensitive sites [63]. In hydrogels that depend on functionalized groups to form crosslinks, SEM demonstrated that the degree of functionalization (DoF) has a greater influence on the pore density, pore size, and porosity percentage than the polymer concentration [90]. For example, high-DoF hydrogels have smaller pores than low-DoF hydrogels at similar polymer concentrations [30,90]. Moreover, both the polymer concentration and DoF have a direct influence on hydrogel swelling (i.e., water retention) and mechanics [63,74,90,91].

The limitations of SEM arise during the hydrogel preparation steps, as visualization requires a dry specimen. Thus, SEM is inherently biased, as desiccation will alter the native microarchitecture. Hydrogel desiccation is commonly achieved by passing a sample through a gradation of alcohol dehydration series [18,37,75–77,92] followed by freeze-drying [38,63,72,74,76,77] or critical point drying [17,37,92]. Thus, desiccation irreversibly alters the microarchitecture, leading to an imprecise hydrogel representation [77]. For example, collagen-HA hydrogels dried at −20 °C, −70 °C, and –196 °C showed variable (mean) pore sizes of 230, 90, and 40 μm, respectively [38]. Methods of applying fixatives such as glutaraldehyde [17,92] or combining with paraformaldehyde have been reported [20,37] for both cell-free and cell-loaded materials, but it is not clear to what extent

the artefacts are prevented. Such artefacts can destroy finer features and leach out ions of interest [93]. Hydrogels are non-conductive, requiring irreversible carbon or metal coating (e.g., Au-Pd) [17,20,37,38,74,76] that could conceal finer surface details [93]. Despite these drawbacks, SEM data serve as a comparative measure when all hydrogels sustain the same systematic processing error. Moreover, SEM specimens can be preserved and visualized repeatedly, unlike samples imaged in other electron-based techniques, such as cryogenic SEM (Cryo-SEM) or environmental SEM (ESEM).

2.2. Cryogenic Scanning Electron Microscopy

Cryogenic scanning electron microscopy (Cryo-SEM) relies on a standard SEM with a field emission electron gun but employs a cryo-transfer system, where samples can be coated, fractured, and sublimated. In Cryo-SEM, samples must undergo vitrification: an ultra-rapid freezing method that prevents water crystal formation and generates a glass like-specimen [94]. The most widely reported method of vitrification in hydrogels is by plunge freezing either in liquid nitrogen, liquid ethane, liquid propane, or nitrogen slush at −137 °C [77,95–97]. Post-vitrification metal coating is not deemed essential but improves the imaging resolution [95]. Specimens can be fractured in order to visualize their inner-most microarchitecture and sublimated to remove the top layer of water, revealing the underlying microarchitecture [98]. The fast freezing step preserves biological structures with a higher fidelity than conventional SEM, rendering the Cryo-SEM imaging more factual in order to evaluate the hydrogel pore size [95], porosity [99], and fiber diameter (Figure 2) [98,99]. The presence of cells can also be detected [100,101]. As in SEM, most limitations of Cryo-SEM arise during the sample preparation stage. While, in principle, vitrification prevents ice crystallization, this process depends on a high cooling rate, which is difficult to achieve in specimens with a >10 μm thickness. The use of high-pressure freezing (Figure 2), which consists of a stream of liquid nitrogen at a rate of >2000 bar (~1.5×10^6 Torr) pressure can reportedly vitrify samples of a ⩽500 μm thickness at −196 °C [94]. A poor cryo-fixation generates hexagonal ice crystals that displace the polymer network, causing structural damage [95]. Adding cryoprotectants improves the vitrification process, although the effective concentrations have been reported as cytotoxic upon prolonged exposure [97]. It is unclear whether cytotoxicity would cause any real alterations to cell-loaded specimens, as this step is performed immediately before freezing. Sublimation reportedly caused cracks on the surfaces of alginate hydrogels [95], and these are likely to occur in other polymer networks as well. Slow freezing rates are also reported, while sample dehydration and architecture distortion are common artefacts [95,96]. Compared to SEM, fewer studies report on the use of Cryo-SEM for hydrogels. For a detailed guide on hydrogel preparation for Cryo-SEM, the reader is directed elsewhere [95].

2.3. Environmental Scanning Electron Microscopy

ESEM is another electron-based mode, with the particularity that vacuum conditions allow for the presence of water vapor inside the imaging chamber [79]. In ESEM, the electron gun is kept at a short distance from the sample to reduce vapor interference. As secondary electrons are emitted, their collision with gas molecules amplifies the signal detection. Hence, water vapor not only hydrates the sample, but also plays a key role in image generation [79]. Two modalities of ESEM are available, a wet mode and a low-vacuum mode [102]. In the wet mode, the vapor pressure remains between 4–6 Torr, and the sample is kept cool at 5 °C. In the low-vacuum mode, the pressure within the chamber remains at 1 Torr, keeping a 5% relative humidity [103]. These imaging conditions render the specimen desiccation and metal coating unnecessary.

As the specimens remain in their native, swollen state, ESEM is regarded as optimal for biological samples (Figure 2) [79,93,104]. Resolution limits in ESEM are slightly lower than those in SEM (50 nm > 10 nm; respectively), but the preservation of the morphological integrity of the specimen is an advantage [78,79,93]. The use of cross-sections to visualize the internal microarchitecture of hydrogels with ESEM has also been reported [105]. De-

spite the clear advantages of ESEM compared to the previously mentioned SEM modes, some limitations are involved. Firstly, the high humidity in the chamber can cause water condensation on the sample surface, impeding visualization [78]. Due to the hydrophilic nature of hydrogels, this is likely to occur. Secondly, despite the humid conditions within the chamber, both the constant voltage and changes in vacuum pressure during imaging will invariably induce artefacts [102,106]. Thirdly, imaging must be performed within a relatively short time frame (<45 min), as the voltage and vacuum will inevitably alter the sample. For this reason, ESEM samples require immediate visualization, unlike SEM specimens that can be stored for later imaging. As with Cryo-SEM, ESEM is regarded as underutilized for hydrogel imaging [95,102,106,107], demonstrating a relevant gap in our knowledge of the microarchitecture of polymer networks in their native wet state.

3. Photon-Based Techniques

3.1. Micro-Computed Tomography

Micro-computed tomography (μ-CT) is an X-ray-based scanning imaging tool that generates 2D trans-axial projections of a specimen [108,109]. While μ-CT is classified in this work as a photon-based technique, X-rays derive from the electron interactions within a high-energy electromagnetic beam [110]. In the μ-CT equipment, the sample is placed on a rotational stage and exposed to an X-ray source, and the passing light is captured by an X-ray detector. The passing X-rays can be attenuated (i.e., absorbed or scattered) by the sample thickness, density, and composition, providing phase contrast to the structures and components [111]. The μ-CT images can be reconstructed in 3D with an up to 1 μm voxel (3D pixel) resolution, making this a high-resolution technique. As an X-ray-based imaging method, μ-CT has historically been reported as a tool for reconstructing bone microarchitecture [112–115]. Studies on cell-loaded and cell-free hydrogels have used this technique to detect hydrogel mineralization both in vitro and in vivo [116–119]. The μ-CT data can be used to determine the pore size and fiber thickness in order to reconstruct the polymer network in 3D, demonstrating the pore interconnectivity [102,108]. Hydrogel degradation tests employing μ-CT in vitro demonstrate an increase in the pore sizes and porosity percentages [105,120–122]. While μ-CT is regarded as both non-destructive and non-invasive, exposure to high current and voltage levels will invariably dehydrate the sample [123]. High voltage levels are common when generating high-resolution images, but they are costly and result in a prolonged imaging time. To prevent structural damage during imaging, some reports recommend specimen fixation or the use of (freeze-)dried samples [116,121]. Thus, it is not uncommon to validate hydrogel μ-CT data using SEM data derived from dry specimens [105,123–125]. There are other limitations of μ-CT, as the hydrophilic nature of hydrogels provides a low-phase separation contrast (Figure 4) [119]. Radiopaque agents can be coupled with the polymer backbone or solubilized and left to soak with the hydrogel to improve said contrast [119]. Contrast agents allow us to discern between the hydrogel fibers and porosity and have been used to investigate hydrogel degradation in vivo and in vitro [126,127]. Reportedly, osmium tetroxide and uranyl acetate, or a combination of uranyl acetate and lead citrate, enabled a good contrast resolution and 3D reconstruction of collagen-I hydrogels [128]. The use of metal nanoparticles (e.g., Au) has also been reported to improve the hydrogel contrast [119] or the visualization of the spatial distribution of the cells within. Other limitations include vibrations in the μ-CT's rotatory stage, which can cause motion artefacts by displacing the sample if it is not properly fixed—a common challenge with wet materials [123]. Information on the in-depth specifications and further limitations of μ-CT in materials research can be found elsewhere [111,123].

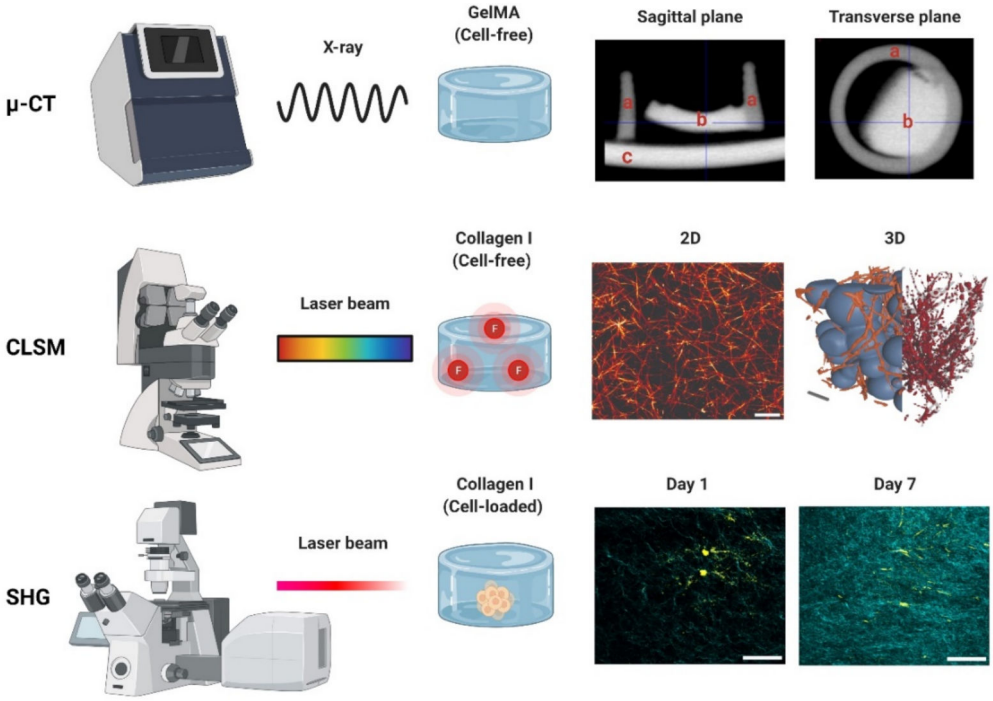

Figure 4. Photon-based imaging techniques. Micro-CT (μ-CT) employs X-rays, creating contrast based on the material properties (e.g., thickness, composition). A GelMA hydrogel scanned with μ-CT is shown in both the sagittal and transverse planes: (a) indicates the PCL container used for casting (2 mm diameter), (b) the GelMA hydrogel, and (c) the stage holder. Confocal laser scanning microscopy (CLSM) employs a laser to excite a fluorophore, which emits the fluorescent signal used for detection. Images of a collagen type-I hydrogel (3 g/L) are shown in 2D and 3D. The 3D image can be used to determine the interconnectivity of the polymer network (orange/red) using a bubble analysis (blue). Scale bars represent 5 μm (2D) and 10 μm (3D). Second harmonic generation (SHG). An example of a cell-loaded (fibroblast) collagen type-I hydrogel is shown on day 1 and day 7. The increase in the SHG signal indicates an increase in the collagen deposition during cell culture. SHG data derived from paraffin-embedded formalin-fixed hydrogels. Scale bars represent 50 μm. μ-CT, CLSM and SHG used to generate the data detailed in Appendix A.

3.2. Confocal Laser Scanning Microscopy

Confocal laser scanning microscopy (CLSM) is a photon-based fluorescent imaging technique. For visualization, CLSM requires that proteins and structures are stained or coupled with fluorophores: organic molecules that can emit light (λ_{em}) upon light excitation (λ_{ex}) [129]. The CLSM optical resolution is determined by the wavelength of the laser. This wavelength is chosen according to the absorption spectra of the fluorophores, and multiple lasers can be used at the same time or in succession to capture multi-color fluorescent images [130]. Unlike conventional fluorescent microscopes that illuminate the entire specimen, CLSM uses point illumination, typically a laser beam, and a pinhole in front of the detector to eliminate most of the background blur, greatly increasing the optical resolution [131]. As only a single point of the specimen is illuminated, the samples must be scanned over a specified region to produce 2D or 3D fluorescent images.

CLSM is an invaluable tool used to visualize the structures of living cells within hydrogels [132]. For the assessment of the hydrogel microarchitecture, these can be fluorescently dyed [58], although certain polymers are naturally auto-fluorescent (e.g., chitosan), allowing dye-free imaging [133]. CLSM yields high-resolution 2D and 3D images (Figure 4), revealing the polymer network microarchitecture in great detail, crucial in the determination of the pore size and porosity of hydrogels in their swollen state (Figure 5) [57–59]. Overall, CLSM agrees with SEM in regards to the pore size decreasing with increasing polymer concentrations [58]. CLSM images can be segmented into a polymer phase and

a fluid phase [42] (Figure 4, orange). During analysis, spheres can be fitted into the fluid phase (Figure 4, blue), and their diameter is measured to determine the pore diameter. The pore diameter, together with the median values of all the detected pore diameters, is defined as the pore size of a particular sample [42]. Applying the same principle to the polymer phase can determine the average thickness of individual fibers (Figure 5A). Additionally, CLSM images can be used to quantify local deviations in the microarchitecture due to nodes formed during the polymerization of collagen-I hydrogels. Moreover, data from fluorescently labelled collagen-I hydrogels showed that fiber diameter and fiber length are heavily influenced by pH, irrespective of the hydrogel concentration. In contrast, the pore size remained unaffected by pH [58].

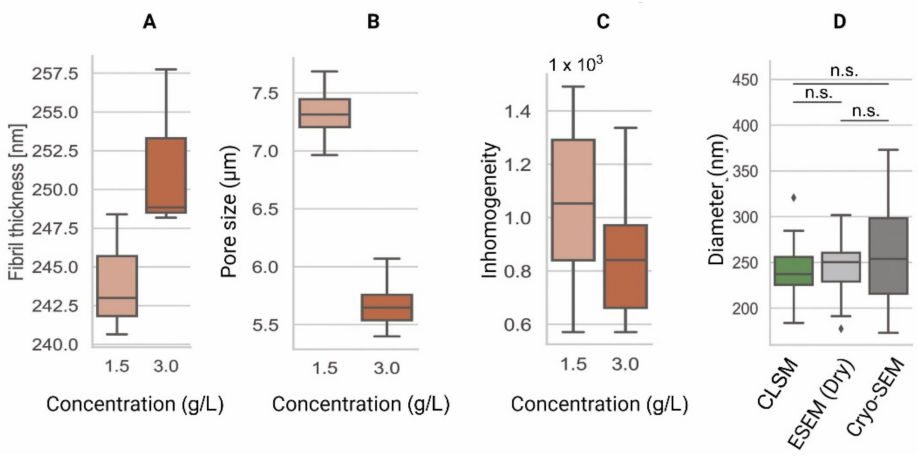

Figure 5. Comparison of the microarchitecture parameters among collagen type-I hydrogels of 1.5 g/L and 3.0 g/L. (**A**) Fiber thickness is an estimation of the 3D cross-sectional diameter of collagen fibers [62]. (**B**) Pore size represents the contiguous 3D space between collagen fibers [42]. (**C**) Inhomogeneity derived from the CLSM data is a measure of local and global variance in the pore size [57]. (**D**) Comparison of pore diameters among CLSM [42], ESEM, and Cryo-SEM images of collagen type-I hydrogels (3.0 g/L). These data indicate similar fiber diameter results among all techniques. Data shown in box-and-whisker plots indicating the median, first and third quartiles as boxes, variability as whiskers and outliers shown as ⬥. n.s. = no significant differences.

Data from CLSM applied to cell-loaded hydrogels can be used to detect local cell-induced microenvironmental changes during migration through an inhomogeneity parameter [57]. This inhomogeneity parameter can explain differences in cell migration that cannot be explained using the pore size and mechanical properties alone. Therefore, elucidating these differences has led to significant insights into the role and adaptation of the microenvironment during cell migration [57].

CLSM has some limitations, the most important being the resolution limit due to optical diffraction limits. CLSM employs lasers with excitation wavelengths of several hundred nanometers, and the excited fluorophores commonly emit light at a higher wavelength. For example, collagen fibers in polymerized matrices possess a wide range of diameters, ranging from below 100 nm [134] to nearly 1 µm [58]. Using a λ_{ex} 561 nm-laser and recording λ_{em} 580 nm, objects as small as 290 nm can be distinguished. Thus, this technique [42] must be considered an overestimation, as the fiber thickness can be below the optical diffraction limit. However, due to multiple post-processing steps, the analysis can be considered as quasi-pixelwise. Another important consideration is the efficacy of the fluorescent dyes used. Poor staining might result in a low signal-to-noise ratio or even the inhomogeneous staining of a hydrogel, resulting in limitations in the dynamic range. Thicker and, thus, brighter fibers may overlay smaller fibrils, or vice versa, with larger fibers losing detail when overexposed. Lastly, the choice of a spherical space estimator might not be suitable for a specific problem. For a robust estimate of the cell migration, spheres can be considered a suitable shape. However, other problems can make it necessary to

choose other shapes, such as cubes. Fitting shapes into the hydrogel segmentation might be entirely superfluous, and polymer content calculations based on the precise segmentation may provide a better parameter.

3.3. Second Harmonic Generation

The higher-order assembly of structural elements (fibrils and fibers) within hydrogels can be examined using non-destructive laser-scanning optical multiphoton microscopy methods [135]. Such techniques are non-linear optical methods that employ femtosecond pulses from near-infrared (NIR) lasers, which enables researchers to examine samples with deeper tissue penetration in comparison to CLSM [136]. The interaction of the femtosecond pulsed NIR light with collagen fibers produces second harmonic generation (SHG) and two-photon excited fluorescence (TPF) signals [137]. The non-absorptive photon interaction with the collagen fibers produces photons with exactly twice the original energy, resulting in an SHG signal that is emitted at exactly half the excitation wavelength. The output signal is dependent on the non-centrosymmetric assembly of the collagen triple helices (secondary structure) and also on the molecular packaging and arrangement of the fibrils (tertiary structure) and the organization of the fibers (quaternary structure) [138]. The TPF signal, on the other hand, is generated through an absorptive process that results from the excitation of inherent fluorophores within the collagen structure (intramolecular pyridinium-type crosslinks and other fluorophores of an unknown nature) [139]. These SHG signals are generated through the specific structural organization of collagens and, therefore, they do not capture information about other mechanically and structurally important elements within the matrix, such as elastin, proteoglycans, and other non-collagenous components. The significant advantage of SHG microscopy is that the signals are generated by the macromolecules, thus obviating the need for staining with fluorophores. SHG has been used to characterize the fiber structural arrangement in collagen hydrogels up to a depth of 1 mm [135,138], and the fiber arrangement, orientation, thickness, and anisotropy have been assessed within hydrogels [140]. Different structural features in collagen hydrogels of a constant concentration that were polymerized under varying pH or temperature conditions can be detected using SHG imaging [138,141]. The measured fiber diameters from SHG images correlate linearly with those from SEM images of the same preparations, although the SEM-calculated diameters are usually smaller due to the dehydration that takes place during the sample preparation [135]. The signal-to-noise ratio for SHG is higher than that observed with TPF, likely due to the quadratic signal of SHG versus the direct concentration dependence of the TPF signal, coupled with the weak auto-fluorescent signal from immature, weakly cross-linked collagen and potentially other ECM molecules, when they are present. This means that homogeneous and incoherent signal emissions can be observed in all fiber orientations using TPF; however, the coherent nature of the SHG signal prevents emission detection when the collagen fibers are orientated parallel to the laser direction [142]. The SHG and TPF signals can provide different information about the structural properties of the collagen hydrogels, e.g., heavily cross-linked collagen in fibrotic tissue and newly deposited collagen. When collagen hydrogels are polymerized under a decreasing temperature, a relationship between the SHG signal and the mechanical properties of the hydrogel can be observed. As the polymerization temperature decreases, the collagen fiber diameter and the pore size detected increase, while the storage modulus G′ and the mean SHG signal decrease. When the crosslinking within the hydrogel is altered using glutaraldehyde, the SHG signal does not change; however, the TPF signal and the storage modulus increase in line with the degree of crosslinking [138]. These data indicate that the SHG and TPF signals impart different information about the characteristics of the collagen hydrogels that correlates with the hydrogel mechanical properties. The detection of forward versus backward SHG signals can provide additional information related to the organization of collagen fibers [143]. Collagen fibers of approximately the same size as the SHG wavelength generate a signal exclusively in the forward direction [136,137,140,144]. In contrast, sites where the fiber thickness changes or fiber interfaces can change the direction

of the emitted SHG signal and generate a backward signal [145]. In cell-free collagen hydrogels, any backward SHG signal detected is the result of the scattering of the forward SHG signal, with a small component of the backwards-generated SHG being generated from small fibrils (diameters ~10% of $\lambda 2\omega$). In collagen hydrogels generated at 27 °C, the degree of the backscattering of the SHG signal to the forward detector increases as the initial hydrogel concentration increases, while for hydrogels assembled at 37 °C, the degree of backscattering is much less, reflecting the shorter, more uniform collagen fiber assembly [135]. SHG signals can also be used to investigate how cells remodel their immediate microenvironment when seeded in collagen hydrogels. Cells seeded in collagen hydrogels remodel and contract the hydrogel, altering the collagen microarchitecture [64,146,147]. The SHG signals indicate that the distinct collagen microstructural properties are still present within the hydrogel even after the gel has contracted, with the signal intensity increasing linearly, reflecting the increased collagen concentration as the hydrogels contract [147]. Overtime, cells can remodel the collagen environment within the hydrogels. The SHG signal indicates that the pore size reduces as the collagen bundles (and presumably other ECM components) become larger. SHG has also been used to investigate collagen remodeling and the role of enzymes released from the cells in crosslinking collagen fibers [148]. Collagen fibers that are newly deposited by cells encapsulated in alginate hydrogels are also readily visualized by SHG [149].

3.4. Atomic Force Microscopy

Atomic force microscopy (AFM) began as a device capable of measuring forces as small as attonewtons [150]. This technique was advanced to record surface heightmaps on the atomic level, resulting in precise measurements of the surface topology of soft samples [151]. This method, also called scanning force microscopy (SFM) [152], eventually became an invaluable tool in biophysics [153]. AFM can demonstrate the hydrogel surface topology, but also the mechanical properties, through the mathematical modelling of the force–distance curves [148,152]. Hence, AFM can determine the cell elasticity [62] and elastic/Young's moduli of hydrogels [57]. The AFM working principle is illustrated in Figure 6A,B, and a topological heightmap of a collagen-I hydrogel is depicted in Figure 6C. AFM sensitivity can include a phase separation analysis, which distinguishes between the distributions of different polymers in co-polymer hydrogel formulations (i.e., more than a single polymer type in a single hydrogel) [108].

AFM can also determine the elastic properties of soft matter, such as hydrogels [58] (Figure 6D), by fitting the cantilever-derived curves (Figure 6E) in different models (e.g., the Hertz model) to calculate the elastic modulus of the hydrogels [57,62], such as collagen type-I (Figure 6F). Hence, the AFM serves not only to characterize the surface topology of a hydrogel, but also to determine its elastic/Young's modulus (i.e., stiffness). However, using the AFM technique to determine the elastic moduli of hydrogels also has limitations. Depending on the actual stiffness of the material, a cantilever with a certain spring constant must be chosen. For example, using a stiff cantilever to probe a soft material will result in a poor signal-to-noise ratio, while using a soft probe for a soft material leads to an optimal signal-to-noise ratio. Vice versa, a soft cantilever might not indent a stiff material.

Depending on the type of hydrogel, the AFM technique can be difficult or even impossible to carry out. Spheroidal probes might stick to the material, resulting in artefacts, disrupted force–distance curves, or even damaged cantilevers. If the cantilever probe is much smaller than the pore size of the hydrogel, it might get stuck in the fibrous network microarchitecture. However, a larger and heavier spheroid influences the spring characteristics of the cantilever. Lastly, the AFM device, in general, is prone to errors due to vibrations, resulting in signal noise and ultimately uncertainties in the Hertz model fit. The usage of vibration dampeners and casings drastically reduces vibrations and are highly recommended. These limitations must be carefully considered when choosing the correct settings to obtain precise measurements.

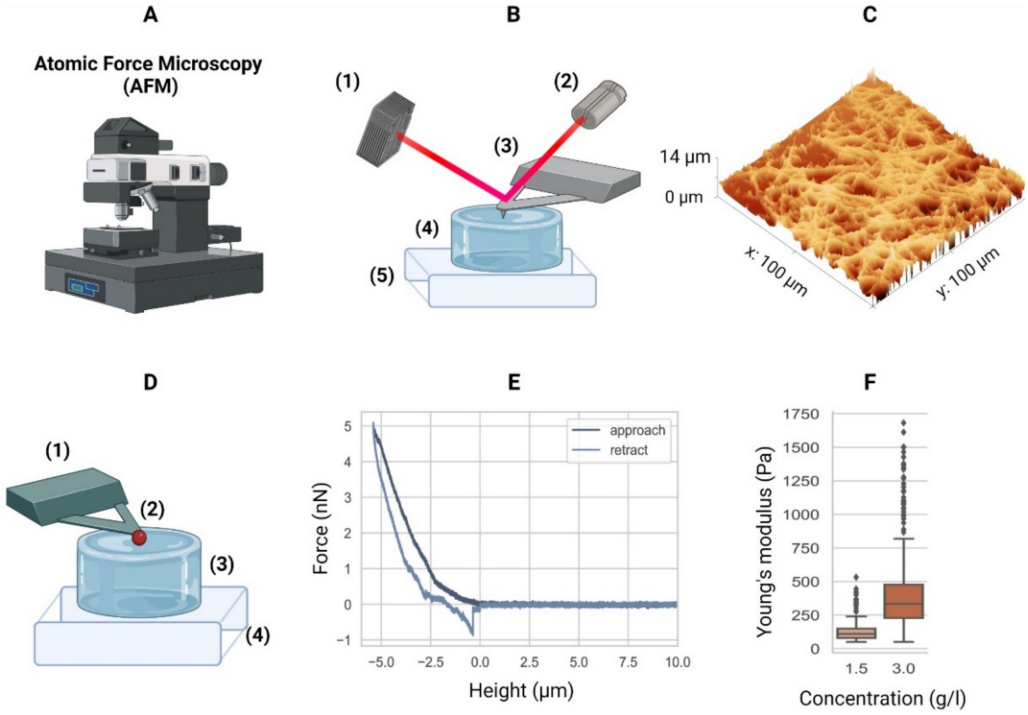

Figure 6. Atomic force microscopy. (**A**) Equipment. (**B**) Schematic of an AFM setup with a four-quadrant photodiode (1), in which the four-quadrant photodiode (1) receives a laser (2) reflected from a cantilever (3), in this case positioned over a hydrogel (4) mounted in a piezo stage (5). For example, the height differences in a sample (4) are measured by adjusting the stage using piezo elements (5) to counter the cantilever bending on a nanometer scale. (**C**) The AFM can then generate a surface heightmap of the hydrogels such as a GelMA hydrogel (shown). AFM can also be used to determine the mechanical properties of hydrogels. (**D**) Schematic of the AFM technique to determine the elastic moduli of hydrogels with a tipless cantilever (1), spheroidal probe (2, red), hydrogel (3), and stiff substrate (4). As the cantilever represents a spring with a known spring constant, the cantilever bending due to elastic counterforces exerted by the soft material is correlated with the piezo stage height (4). (**E**) The so-called force–distance curves are recorded. Data from a collagen type-I hydrogel (3.0 g/L) are shown. (**F**) Young's moduli of a 1.5 g/L and 3.0 g/L collagen type-I hydrogel. Outliers indicated by ⬥. AFM equipment detailed in Appendix A.

4. Hydrogel Microarchitecture and Cells: Design and Applications

Hydrogels are 2D and 3D cell culture platforms that mimic the ECM and are used in 3D bioprinting and the field of tissue engineering and regenerative medicine (TERM) for cell and drug delivery [8,11,85,154,155]. These cellular applications demonstrate the versatility of hydrogels, and therefore, great efforts are being put into moderating their properties, including their microarchitecture. The hydrogel microarchitecture is described in terms of porosity (percentage), pores (distribution, geometry, interconnectivity, and size), and fiber (thickness/diameter, directionality, and length), as well as surface topography. Researchers have recognized the relevance of these microarchitectural components in driving the cell fate and have aimed to modulate them [53,156,157].

The hydrogel microarchitecture can be modulated by manipulating the crosslinking conditions [158] and by adding porogens, such as salt leaching (e.g., NaCl, NaOH) [159] and gas foaming [160]. Other approaches include 3D printing [161], micropatterning [162], and micro-molding [163] to control the hydrogel geometry and desired topography. Ironically, research citing methods for controlling the hydrogel porosity has assessed this property mostly with SEM [156,157], a biased technique, as previously discussed.

Vascularization and cartilage and bone formation are processes of interest in TERM, which are closely linked to hydrogel microarchitecture. Endothelial cell migration and

tissue vascularization were considered optimal in HA-methacrylated (HA-MA) with pore sizes of 200–250 µm [164]. PEG hydrogels with pore size ranges of 50–150 µm facilitated vascularization [165], while GelMA with pores of 49.7 ± 11.8 µm showed capillaries in vitro [62].

PGA scaffolds with a 97% porosity and fiber thickness of 13–15 µm exhibited chondrocyte differentiation [53]. Meanwhile, in genipin-crosslinked gelatin scaffolds, pore sizes between 250–500 µm promoted ECM deposition and chondrocyte proliferation [48].

The osteoblastic differentiation of pluripotent stem cells was reported in hyaluronic acid (HA) hydrogels loaded with bone morphogenetic protein-2 (BMP-2) with pore sizes ranging from 100–600 µm [166]. Human bone marrow stem cells underwent osteoblastic differentiation in silk fibroin scaffolds with ~92% porosity and pore sizes of 920 ± 50 µm [167]. Contrastingly, polycaprolactone (PCL) scaffolds with pore sizes between 300–900 µm had limited effects on the promotion of bone regeneration in vivo [45].

In cancer cell models, cell morphology, cluster formation, and cell invasion are regulated by the fiber diameter (850 nm) and not the pore size (7.5–11 µm) [58]. Thus, the polymer chemistry and the cellular applications, whether in vivo or in vitro, can yield contrasting outcomes. Regardless, the microarchitectural parameters reported here were characterized by the electron-based or photon-based imaging techniques, as previously described. The data generated with said techniques can result in diverse post-processing analyses, some of which can be consulted here [168–170].

5. Conclusions

Mimicking the ECM through the use of hydrogels is an experimental model of increasing interest. In this review, we have highlighted the microarchitecture data that can be acquired by distinct imaging methods. It is important to mention the following: Firstly, most of the characterization thus far has been performed on cell-free hydrogels. This means that we lack an overview of the cell-induced microarchitectural modifications of hydrogels over time. Secondly, the hydrophilic nature of hydrogels poses a real challenge for the characterization of their microarchitecture, topography, and other mechanical parameters briefly mentioned here, such as stiffness (i.e., elastic/Young's modulus) and viscoelasticity [91,95]. Thirdly, many of the described techniques are considered non-destructive, but on closer inspection, this only applies to the test phase and not to the sample preparation, which can often lead to significant changes in the hydrogels. Finally, the limitations reported here are not solely technical, but also pertain to the inconsistent interpretation and reporting of the applied parameters [112,171]. There is a clear need to standardize the minimum reporting criteria employed for data acquisition. Thus far, the absence of clear concept definitions, alongside poorly described methods, hinders experimental reproducibility. Adequate reporting, as well as the development of novel biophysical tools, will lead to a deeper understanding of cell–matrix biology in hydrogel systems.

Author Contributions: Conceptualization, F.D.M.-G., T.F., A.H., C.T.M., J.K.B. and M.C.H.; methodology, F.D.M.-G., T.F. and A.H.; investigation, formal analysis and writing—original draft, F.D.M.-G., T.F., A.H. and J.K.B.; validation, F.D.M.-G. and T.F.; writing—review & editing and supervision, C.T.M., J.K.B. and M.C.H.; funding acquisition, F.D.M.-G., J.K.B. and M.C.H.; visualization F.D.M.-G. All authors have read and agreed to the published version of the manuscript.

Funding: This project was supported by the Mexican National Council of Science and Technology (CONACyT; CVU 695528) and by the De Cock-Hadders Foundation (2021-16). J.K. Burgess was supported by a Rosalind Franklin Fellowship co-funded by the University of Groningen and the European Union.

Institutional Review Board Statement: Not applicable.

Informed Consent Statement: Not applicable.

Data Availability Statement: All data presented in this work are available upon reasonable request.

Acknowledgments: We acknowledge Ana Isabel Sariol for her support in the literature search. SEM images of collagen-I hydrogels were generated with the support of Gert ten Brink at the Faculty of Science and Engineering, University of Groningen. We thank Jeroen Kuipers for the SEM-EDX images generated at the UMCG Microscopy and Imaging Center (UMIC). We also recognize Britt van Akker for generating the μ-CT data. The figure designs were created with BioRender.com.

Conflicts of Interest: The funders had no role in the design of the study; in the collection, analyses, or interpretation of data; in the writing of the manuscript; or in the decision to publish the results.

Appendix A

Collagen-I hydrogels (3.0 g/L) shown in Figures 2–6 were prepared as described here [43]. For the CLSM imaging, the collagen-I hydrogels were polymerized on top of a functionalized glass-coverslip and coated with (3-Aminopropyl)trimethoxysilane (APTMS; Sigma Aldrich, St Louis, MO, USA). The GelMA hydrogels (5% w/v) shown in Figures 3 and 4 are derived from the same batch reported here [93], with a 56.0 ± 0.9% DoF according to nuclear magnetic resonance.

The HUVECs shown in Figure 3 were cultured in RPMI 1640 (Lonza, Verviers, Belgium) supplemented with 20% FBS (Gibco, Paisley, UK), 1% Pen-Strep (Gibco), 2 mM L-Glut (BioWhittaker, Walkersville, MD, USA), 5 U/mL Heparin (Leo Pharma, Amsterdam, the Netherlands), and 50 μg/mL crude endothelial cell growth factor (Roche, Mannheim, Germany).

The data presented in this review were obtained with the following instruments: SEM-Zeiss Supra 55 STEM (Carl Zeiss NTS GmbH, Oberkochen, Germany); Cryo-SEM and ESEM-Quanta 200 FEG (Philips-FEI, Hillsboro, OR, USA); μCT-Inveon PET/CT (Siemens Medical Solutions USA, Knoxville, TN, USA); CLSM-Zeiss LSM 780 (Carl Zeiss NTS GmbH, Oberkochen, Germany); SHG-SP5 multiphoton (Leica, Amsterdam, The Netherlands); and AFM-JPK CellHesion® R200 (Bruker Nano GmbH, Berlin, Germany) with Arrow-TL2-50 cantilevers (Nano-World®, Neuchâtel, Switzerland) and polystyrene beads glued to them. All data shown are original and were not published elsewhere.

References

1. Frantz, C.; Stewart, K.M.; Weaver, V.M. The Extracellular Matrix at a Glance. *J. Cell Sci.* **2010**, *123*, 4195–4200. [CrossRef]
2. Couchman, J.R.; Pataki, C.A. An Introduction to Proteoglycans and Their Localization. *J. Histochem. Cytochem.* **2012**, *60*, 885–897. [CrossRef]
3. Pethig, R.; Kell, D.B. The Passive Electrical Properties of Biological Systems: Their Significance in Physiology, Biophysics and Biotechnology. *Phys. Med. Biol.* **1987**, *32*, 933–970. [CrossRef]
4. Ahmed, E.M. Hydrogel: Preparation, Characterization, and Applications: A Review. *J. Adv. Res.* **2015**, *6*, 105–121. [CrossRef]
5. Pita-López, M.L.; Fletes-Vargas, G.; Espinosa-Andrews, H.; Rodríguez-Rodríguez, R. Physically Cross-Linked Chitosan-Based Hydrogels for Tissue Engineering Applications: A State-of-the-Art Review. *Eur. Polym. J.* **2021**, *145*, 110176. [CrossRef]
6. Lang, N.R.; Skodzek, K.; Hurst, S.; Mainka, A.; Steinwachs, J.; Schneider, J.; Aifantis, K.E.; Fabry, B. Biphasic Response of Cell Invasion to Matrix Stiffness in Three-Dimensional Biopolymer Networks. *Acta Biomater.* **2015**, *13*, 61–67. [CrossRef]
7. Paszek, M.J.; Zahir, N.; Johnson, K.R.; Lakins, J.N.; Rozenberg, G.I.; Gefen, A.; Reinhart-King, C.A.; Margulies, S.S.; Dembo, M.; Boettiger, D.; et al. Tensional Homeostasis and the Malignant Phenotype. *Cancer Cell* **2005**, *8*, 241–254. [CrossRef]
8. Li, Y.; Kilian, K.A. Bridging the Gap: From 2D Cell Culture to 3D Microengineered Extracellular Matrices. *Adv. Healthc. Mater.* **2015**, *4*, 2780–2796. [CrossRef] [PubMed]
9. Tibbitt, M.W.; Anseth, K.S. Hydrogels as Extracellular Matrix Mimics for 3D Cell Culture. *Biotechnol. Bioeng.* **2009**, *103*, 655–663. [CrossRef]
10. Tsou, Y.H.; Khoneisser, J.; Huang, P.C.; Xu, X. Hydrogel as a Bioactive Material to Regulate Stem Cell Fate. *Bioact. Mater.* **2016**, *1*, 39–55. [CrossRef]
11. Ruedinger, F.; Lavrentieva, A.; Blume, C.; Pepelanova, I.; Scheper, T. Hydrogels for 3D Mammalian Cell Culture: A Starting Guide for Laboratory Practice. *Appl. Microbiol. Biotechnol.* **2015**, *99*, 623–636. [CrossRef]
12. Stanton, M.M.; Samitier, J.; Sánchez, S. Bioprinting of 3D Hydrogels. *Lab A Chip* **2015**, *15*, 3111–3115. [CrossRef] [PubMed]
13. Kim, H.-D.; Guo, T.W.; Wu, A.P.; Wells, A.; Gertler, F.B.; Lauffenburger, D.A. Epidermal Growth Factor–Induced Enhancement of Glioblastoma Cell Migration in 3D Arises from an Intrinsic Increase in Speed But an Extrinsic Matrix- and Proteolysis-Dependent Increase in Persistence. *Mol. Biol. Cell* **2008**, *19*, 4249–4259. [CrossRef] [PubMed]

14. De Hilster, R.H.J.; Sharma, P.K.; Jonker, M.R.; White, E.S.; Gercama, E.A.; Roobeek, M.; Timens, W.; Harmsen, M.C.; Hylkema, M.N.; Burgess, J.K. Human Lung Extracellular Matrix Hydrogels Resemble the Stiffness and Viscoelasticity of Native Lung Tissue. *Am. J. Physiol. -Lung Cell. Mol. Physiol.* **2020**, *318*, L698–L704. [CrossRef] [PubMed]
15. Liguori, G.R.; Liguori, T.T.A.; de Moraes, S.R.; Sinkunas, V.; Terlizzi, V.; van Dongen, J.A.; Sharma, P.K.; Moreira, L.F.P.; Harmsen, M.C. Molecular and Biomechanical Clues From Cardiac Tissue Decellularized Extracellular Matrix Drive Stromal Cell Plasticity. *Front. Bioeng. Biotechnol.* **2020**, *8*, 520. [CrossRef]
16. Dongen, J.A.; Getova, V.; Brouwer, L.A.; Liguori, G.R.; Sharma, P.K.; Stevens, H.P.; Lei, B.; Harmsen, M.C. Adipose Tissue-derived Extracellular Matrix Hydrogels as a Release Platform for Secreted Paracrine Factors. *J. Tissue Eng. Regen. Med.* **2019**, *13*, 973–985. [CrossRef]
17. Freytes, D.O.; Martin, J.; Velankar, S.S.; Lee, A.S.; Badylak, S.F. Preparation and Rheological Characterization of a Gel Form of the Porcine Urinary Bladder Matrix. *Biomaterials* **2008**, *29*, 1630–1637. [CrossRef]
18. Sackett, S.D.; Tremmel, D.M.; Ma, F.; Feeney, A.K.; Maguire, R.M.; Brown, M.E.; Zhou, Y.; Li, X.; O'Brien, C.; Li, L.; et al. Extracellular Matrix Scaffold and Hydrogel Derived from Decellularized and Delipidized Human Pancreas. *Sci. Rep.* **2018**, *8*, 10452. [CrossRef]
19. Catoira, M.C.; Fusaro, L.; Di Francesco, D.; Ramella, M.; Boccafoschi, F. Overview of Natural Hydrogels for Regenerative Medicine Applications. *J. Mater. Sci. Mater. Med.* **2019**, *30*, 115. [CrossRef]
20. Martinez-Garcia, F.D.; de Hilster, R.H.J.; Sharma, P.K.; Borghuis, T.; Hylkema, M.N.; Burgess, J.K.; Harmsen, M.C. Architecture and Composition Dictate Viscoelastic Properties of Organ-Derived Extracellular Matrix Hydrogels. *Polymers* **2021**, *13*, 3113. [CrossRef]
21. Wang, Y.; Zhao, Q.; Zhang, H.; Yang, S.; Jia, X. A Novel Poly(Amido Amine)-Dendrimer-Based Hydrogel as a Mimic for the Extracellular Matrix. *Adv. Mater.* **2014**, *26*, 4163–4167. [CrossRef] [PubMed]
22. Collier, J.H.; Segura, T. Evolving the Use of Peptides as Components of Biomaterials. *Biomaterials* **2011**, *32*, 4198–4204. [CrossRef] [PubMed]
23. Ki, C.S.; Lin, T.-Y.; Korc, M.; Lin, C.-C. Thiol-Ene Hydrogels as Desmoplasia-Mimetic Matrices for Modeling Pancreatic Cancer Cell Growth, Invasion, and Drug Resistance. *Biomaterials* **2014**, *35*, 9668–9677. [CrossRef] [PubMed]
24. Krishnamoorthy, S.; Noorani, B.; Xu, C. Effects of Encapsulated Cells on the Physical–Mechanical Properties and Microstructure of Gelatin Methacrylate Hydrogels. *Int. J. Mol. Sci.* **2019**, *20*, 5061. [CrossRef] [PubMed]
25. Loessner, D.; Meinert, C.; Kaemmerer, E.; Martine, L.C.; Yue, K.; Levett, P.A.; Klein, T.J.; Melchels, F.P.W.; Khademhosseini, A.; Hutmacher, D.W. Functionalization, Preparation and Use of Cell-Laden Gelatin Methacryloyl-Based Hydrogels as Modular Tissue Culture Platforms. *Nat. Protoc.* **2016**, *11*, 727–746. [CrossRef] [PubMed]
26. Yoon, H.J.; Shin, S.R.; Cha, J.M.; Lee, S.H.; Kim, J.H.; Do, J.T.; Song, H.; Bae, H. Cold Water Fish Gelatin Methacryloyl Hydrogel for Tissue Engineering Application. *PLoS ONE* **2016**, *11*, 1–18. [CrossRef]
27. Li, X.; Zhang, J.; Kawazoe, N.; Chen, G. Fabrication of Highly Crosslinked Gelatin Hydrogel and Its Influence on Chondrocyte Proliferation and Phenotype. *Polymers* **2017**, *9*, 309. [CrossRef]
28. Kessler, L.; Gehrke, S.; Winnefeld, M.; Huber, B.; Hoch, E.; Walter, T.; Wyrwa, R.; Schnabelrauch, M.; Schmidt, M.; Kückelhaus, M.; et al. Methacrylated Gelatin/Hyaluronan-Based Hydrogels for Soft Tissue Engineering. *J. Tissue Eng.* **2017**, *8*, 204173141774415. [CrossRef]
29. Camci-Unal, G.; Cuttica, D.; Annabi, N.; Demarchi, D.; Khademhosseini, A. Synthesis and Characterization of Hybrid Hyaluronic Acid-Gelatin Hydrogels. *Biomacromolecules* **2013**, *14*, 1085–1092. [CrossRef]
30. Sun, M.; Sun, X.; Wang, Z.; Guo, S.; Yu, G.; Yang, H. Synthesis and Properties of Gelatin Methacryloyl (GelMA) Hydrogels and Their Recent Applications in Load-Bearing Tissue. *Polymers* **2018**, *10*, 1290. [CrossRef]
31. Yin, J.; Yan, M.; Wang, Y.; Fu, J.; Suo, H. 3D Bioprinting of Low-Concentration Cell-Laden Gelatin Methacrylate (GelMA) Bioinks with a Two-Step Cross-Linking Strategy. *ACS Appl. Mater. Interfaces* **2018**, *10*, 6849–6857. [CrossRef] [PubMed]
32. Pepelanova, I.; Kruppa, K.; Scheper, T.; Lavrentieva, A. Gelatin-Methacryloyl (GelMA) Hydrogels with Defined Degree of Functionalization as a Versatile Toolkit for 3D Cell Culture and Extrusion Bioprinting. *Bioengineering* **2018**, *5*, 55. [CrossRef] [PubMed]
33. Madduma-Bandarage, U.S.K.; Madihally, S.V. Synthetic Hydrogels: Synthesis, Novel Trends, and Applications. *J. Appl. Polym. Sci.* **2021**, *138*, 50376. [CrossRef]
34. Chaudhuri, O.; Gu, L.; Klumpers, D.; Darnell, M.; Bencherif, S.A.; Weaver, J.C.; Huebsch, N.; Lee, H.; Lippens, E.; Duda, G.N.; et al. Hydrogels with Tunable Stress Relaxation Regulate Stem Cell Fate and Activity. *Nat. Mater.* **2015**, *15*, 326. [CrossRef] [PubMed]
35. Chaudhuri, O.; Gu, L.; Darnell, M.; Klumpers, D.; Bencherif, S.A.; Weaver, J.C.; Huebsch, N.; Mooney, D.J. Substrate Stress Relaxation Regulates Cell Spreading. *Nat. Commun.* **2015**, *6*, 6365. [CrossRef]
36. Wisdom, K.M.; Adebowale, K.; Chang, J.; Lee, J.Y.; Nam, S.; Desai, R.; Rossen, N.S.; Rafat, M.; West, R.B.; Hodgson, L.; et al. Matrix Mechanical Plasticity Regulates Cancer Cell Migration through Confining Microenvironments. *Nat. Commun.* **2018**, *9*, 4144. [CrossRef]
37. Laronda, M.M.; Rutz, A.L.; Xiao, S.; Whelan, K.A.; Duncan, F.E.; Roth, E.W.; Woodruff, T.K.; Shah, R.N. A Bioprosthetic Ovary Created Using 3D Printed Microporous Scaffolds Restores Ovarian Function in Sterilized Mice. *Nat. Commun.* **2017**, *8*, 15261. [CrossRef]

38. Park, S.-N.; Park, J.-C.; Kim, H.O.; Song, M.J.; Suh, H. Characterization of Porous Collagen/Hyaluronic Acid Scaffold Modified by 1-Ethyl-3-(3-Dimethylaminopropyl)Carbodiimide Cross-Linking. *Biomaterials* **2002**, *23*, 1205–1212. [CrossRef]
39. Caliari, S.R.; Burdick, J.A. A Practical Guide to Hydrogels for Cell Culture. *Nat. Methods* **2016**, *13*, 405–414. [CrossRef]
40. Karageorgiou, V.; Kaplan, D. Porosity of 3D Biomaterial Scaffolds and Osteogenesis. *Biomaterials* **2005**, *26*, 5474–5491. [CrossRef]
41. León y León, C.A. New Perspectives in Mercury Porosimetry. *Adv. Colloid Interface Sci.* **1998**, *76–77*, 341–372. [CrossRef]
42. Fischer, T.; Hayn, A.; Mierke, C.T. Fast and Reliable Advanced Two-Step Pore-Size Analysis of Biomimetic 3D Extracellular Matrix Scaffolds. *Sci. Rep.* **2019**, *9*, 8352. [CrossRef] [PubMed]
43. Doyle, A.D.; Carvajal, N.; Jin, A.; Matsumoto, K.; Yamada, K.M. Local 3D Matrix Microenvironment Regulates Cell Migration through Spatiotemporal Dynamics of Contractility-Dependent Adhesions. *Nat. Commun.* **2015**, *6*, 8720. [CrossRef] [PubMed]
44. Takahashi, Y.; Tabata, Y. Effect of the Fiber Diameter and Porosity of Non-Woven PET Fabrics on the Osteogenic Differentiation of Mesenchymal Stem Cells. *J. Biomater. Sci. Polym. Ed.* **2004**, *15*, 41–57. [CrossRef]
45. Roosa, S.M.M.; Kemppainen, J.M.; Moffitt, E.N.; Krebsbach, P.H.; Hollister, S.J. The Pore Size of Polycaprolactone Scaffolds Has Limited Influence on Bone Regeneration in an *in Vivo* Model. *J. Biomed. Mater. Res.* **2010**, *92A*, 359–368. [CrossRef]
46. Ho, S.T.; Hutmacher, D.W. A Comparison of Micro CT with Other Techniques Used in the Characterization of Scaffolds. *Biomaterials* **2006**, *27*, 1362–1376. [CrossRef]
47. Kuboki, Y.; Takita, H.; Kobayashi, D.; Tsuruga, E.; Inoue, M.; Murata, M.; Nagai, N.; Dohi, Y.; Ohgushi, H. BMP-Induced Osteogenesis on the Surface of Hydroxyapatite with Geometrically Feasible and Nonfeasible Structures: Topology of Osteogenesis. *J. Biomed. Mater. Res.* **1998**, *39*, 190–199. [CrossRef]
48. Lien, S.-M.; Ko, L.-Y.; Huang, T.-J. Effect of Pore Size on ECM Secretion and Cell Growth in Gelatin Scaffold for Articular Cartilage Tissue Engineering. *Acta Biomater.* **2009**, *5*, 670–679. [CrossRef]
49. Mikos, A.G.; Sarakinos, G.; Lyman, M.D.; Ingber, D.E.; Vacanti, J.P.; Langer, R. Prevascularization of Porous Biodegradable Polymers. *Biotechnol. Bioeng.* **1993**, *42*, 716–723. [CrossRef]
50. Chang, Y.-S.; Gu, H.-O.; Kobayashi, M.; Oka, M. Influence of Various Structure Treatments on Histological Fixation of Titanium Implants. *J. Arthroplast.* **1998**, *13*, 816–825. [CrossRef]
51. Steflik, D.E.; Corpe, R.S.; Young, T.R.; Sisk, A.L.; Parr, G.R. The Biologic Tissue Responses to Uncoated and Coated Implanted Biomaterials. *Adv. Dent. Res.* **1999**, *13*, 27–33. [CrossRef] [PubMed]
52. Yuan, H.; Kurashina, K.; de Bruijn, J.D.; Li, Y.; de Groot, K.; Zhang, X. A Preliminary Study on Osteoinduction of Two Kinds of Calcium Phosphate Ceramics. *Biomaterials* **1999**, *20*, 1799–1806. [CrossRef]
53. Freed, L.E.; Vunjak-Novakovic, G.; Biron, R.J.; Eagles, D.B.; Lesnoy, D.C.; Barlow, S.K.; Langer, R. Biodegradable Polymer Scaffolds for Tissue Engineering. *Nat. Biotechnol.* **1994**, *12*, 689–693. [CrossRef] [PubMed]
54. Stein, A.M.; Vader, D.A.; Jawerth, L.M.; Weitz, D.A.; Sander, L.M. An Algorithm for Extracting the Network Geometry of Three-Dimensional Collagen Gels. *J. Microsc.* **2008**, *232*, 463–475. [CrossRef]
55. Xu, T.; Vavylonis, D.; Tsai, F.-C.; Koenderink, G.H.; Nie, W.; Yusuf, E.; Lee, I.-J.; Wu, J.-Q.; Huang, X. SOAX: A Software for Quantification of 3D Biopolymer Networks. *Sci. Rep.* **2015**, *5*, 9081. [CrossRef] [PubMed]
56. Franke, K.; Sapudom, J.; Kalbitzer, L.; Anderegg, U.; Pompe, T. Topologically Defined Composites of Collagen Types I and V as in Vitro Cell Culture Scaffolds. *Acta Biomater.* **2014**, *10*, 2693–2702. [CrossRef]
57. Hayn, A.; Fischer, T.; Mierke, C.T. Inhomogeneities in 3D Collagen Matrices Impact Matrix Mechanics and Cancer Cell Migration. *Front. Cell Dev. Biol.* **2020**, *8*, 593879. [CrossRef]
58. Sapudom, J.; Rubner, S.; Martin, S.; Kurth, T.; Riedel, S.; Mierke, C.T.; Pompe, T. The Phenotype of Cancer Cell Invasion Controlled by Fibril Diameter and Pore Size of 3D Collagen Networks. *Biomaterials* **2015**, *52*, 367–375. [CrossRef]
59. Fischer, T.; Wilharm, N.; Hayn, A.; Mierke, C.T. Matrix and Cellular Mechanical Properties Are the Driving Factors for Facilitating Human Cancer Cell Motility into 3D Engineered Matrices. *Converg. Sci. Phys. Oncol.* **2017**, *3*, 044003. [CrossRef]
60. Kunschmann, T.; Puder, S.; Fischer, T.; Steffen, A.; Rottner, K.; Mierke, C.T. The Small GTPase Rac1 Increases Cell Surface Stiffness and Enhances 3D Migration Into Extracellular Matrices. *Sci. Rep.* **2019**, *9*, 7675. [CrossRef]
61. Mierke, C.T.; Fischer, T.; Puder, S.; Kunschmann, T.; Soetje, B.; Ziegler, W.H. Focal Adhesion Kinase Activity Is Required for Actomyosin Contractility-Based Invasion of Cells into Dense 3D Matrices. *Sci. Rep.* **2017**, *7*, 42780. [CrossRef] [PubMed]
62. Fischer, T.; Hayn, A.; Mierke, C.T. Effect of Nuclear Stiffness on Cell Mechanics and Migration of Human Breast Cancer Cells. *Front. Cell Dev. Biol.* **2020**, *8*, 393. [CrossRef] [PubMed]
63. Chen, Y.; Lin, R.; Qi, H.; Yang, Y.; Bae, H.; Melero-Martin, J.M.; Khademhosseini, A. Functional Human Vascular Network Generated in Photocrosslinkable Gelatin Methacrylate Hydrogels. *Adv. Funct. Mater.* **2012**, *22*, 2027–2039. [CrossRef]
64. Toki, F.; Honkura, N.; Shirakata, Y.; Imamura, T.; Higashiyama, S.; Nanba, D. Second Harmonic Generation Reveals Collagen Fibril Remodeling in Fibroblast-Populated Collagen Gels. *Cell Struct. Funct.* **2013**, *38*, 229–238. [CrossRef] [PubMed]
65. De Vicente, G.; Lensen, M.C. Topographically and Elastically Micropatterned PEG-Based Hydrogels to Control Cell Adhesion and Migration. *Eur. Polym. J.* **2016**, *78*, 290–301. [CrossRef]
66. Almonacid Suarez, A.M.; van der Ham, I.; Brinker, M.G.L.; van Rijn, P.; Harmsen, M.C. Topography-Driven Alterations in Endothelial Cell Phenotype and Contact Guidance. *Heliyon* **2020**, *6*, e04329. [CrossRef]
67. Al-Haque, S.; Miklas, J.W.; Feric, N.; Chiu, L.L.Y.; Chen, W.L.K.; Simmons, C.A.; Radisic, M. Hydrogel Substrate Stiffness and Topography Interact to Induce Contact Guidance in Cardiac Fibroblasts. *Macromol. Biosci.* **2012**, *12*, 1342–1353. [CrossRef]

68. Almonacid Suarez, A.M.; Brinker, M.G.L.; Brouwer, L.A.; van der Ham, I.; Harmsen, M.C.; van Rijn, P. Topography-Mediated Myotube and Endothelial Alignment, Differentiation, and Extracellular Matrix Organization for Skeletal Muscle Engineering. *Polymers* **2020**, *12*, 1948. [CrossRef]
69. Almonacid Suarez, A.M.; Zhou, Q.; Rijn, P.; Harmsen, M.C. Directional Topography Gradients Drive Optimum Alignment and Differentiation of Human Myoblasts. *J. Tissue Eng. Regen. Med.* **2019**, *13*, 2234–2245. [CrossRef]
70. Chavda, H.; Modhia, I.; Patel, R.; Patel, C. Preparation and Characterization of Superporous Hydrogel Based on Different Polymers. *Int. J. Pharm. Investig.* **2012**, *2*, 134. [CrossRef]
71. Van Vlierberghe, S.; Cnudde, V.; Dubruel, P.; Masschaele, B.; Cosijns, A.; de Paepe, I.; Jacobs, P.J.S.; van Hoorebeke, L.; Remon, J.P.; Schacht, E. Porous Gelatin Hydrogels: 1. Cryogenic Formation and Structure Analysis. *Biomacromolecules* **2007**, *8*, 331–337. [CrossRef]
72. Xiao, W.; He, J.; Nichol, J.W.; Wang, L.; Hutson, C.B.; Wang, B.; Du, Y.; Fan, H.; Khademhosseini, A. Synthesis and Characterization of Photocrosslinkable Gelatin and Silk Fibroin Interpenetrating Polymer Network Hydrogels. *Acta Biomater.* **2011**, *7*, 2384–2393. [CrossRef]
73. Choi, S.-W.; Xie, J.; Xia, Y. Chitosan-Based Inverse Opals: Three-Dimensional Scaffolds with Uniform Pore Structures for Cell Culture. *Adv. Mater.* **2009**, *21*, 2997–3001. [CrossRef]
74. Eke, G.; Mangir, N.; Hasirci, N.; MacNeil, S.; Hasirci, V. Development of a UV Crosslinked Biodegradable Hydrogel Containing Adipose Derived Stem Cells to Promote Vascularization for Skin Wounds and Tissue Engineering. *Biomaterials* **2017**, *129*, 188–198. [CrossRef]
75. Habib, A.; Sathish, V.; Mallik, S.; Khoda, B. 3D Printability of Alginate-Carboxymethyl Cellulose Hydrogel. *Materials* **2018**, *11*, 454. [CrossRef]
76. Jia, W.; Gungor-Ozkerim, P.S.; Zhang, Y.S.; Yue, K.; Zhu, K.; Liu, W.; Pi, Q.; Byambaa, B.; Dokmeci, M.R.; Shin, S.R.; et al. Direct 3D Bioprinting of Perfusable Vascular Constructs Using a Blend Bioink. *Biomaterials* **2016**, *106*, 58–68. [CrossRef]
77. Koch, M.; Włodarczyk-Biegun, M.K. Faithful Scanning Electron Microscopic (SEM) Visualization of 3D Printed Alginate-Based Scaffolds. *Bioprinting* **2020**, *20*, e00098. [CrossRef]
78. Doucet, F.J.; Lead, J.R.; Maguire, L.; Achterberg, E.P.; Millward, G.E. Visualisation of Natural Aquatic Colloids and Particles–A Comparison of Conventional High Vacuum and Environmental Scanning Electron Microscopy. *J. Environ. Monitor.* **2005**, *7*, 115. [CrossRef]
79. Donald, A.M. The Use of Environmental Scanning Electron Microscopy for Imaging Wet and Insulating Materials. *Nat. Mater.* **2003**, *2*, 511–516. [CrossRef]
80. Zheng, H.; Tian, W.; Yan, H.; Yue, L.; Zhang, Y.; Han, F.; Chen, X.; Li, Y. Rotary Culture Promotes the Proliferation of MCF-7 Cells Encapsulated in Three-Dimensional Collagen–Alginate Hydrogels via Activation of the ERK1/2-MAPK Pathway. *Biomed. Mater.* **2012**, *7*, 015003. [CrossRef]
81. Liang, R.; Yang, G.; Kim, K.E.; D'Amore, A.; Pickering, A.N.; Zhang, C.; Woo, S.L.-Y. Positive Effects of an Extracellular Matrix Hydrogel on Rat Anterior Cruciate Ligament Fibroblast Proliferation and Collagen MRNA Expression. *J. Orthop. Transl.* **2015**, *3*, 114–122. [CrossRef]
82. Eslami, M.; Vrana, N.E.; Zorlutuna, P.; Sant, S.; Jung, S.; Masoumi, N.; Khavari-Nejad, R.A.; Javadi, G.; Khademhosseini, A. Fiber-Reinforced Hydrogel Scaffolds for Heart Valve Tissue Engineering. *J. Biomater. Appl.* **2014**, *29*, 399–410. [CrossRef]
83. Zhong, X.; Ji, C.; Chan, A.K.L.; Kazarian, S.G.; Ruys, A.; Dehghani, F. Fabrication of Chitosan/Poly(ε-Caprolactone) Composite Hydrogels for Tissue Engineering Applications. *J. Mater. Sci. Mater. Med.* **2011**, *22*, 279–288. [CrossRef]
84. Patiño Vargas, M.I.; Martinez-Garcia, F.D.; Offens, F.; Becerra, N.Y.; Restrepo, L.M.; van der Mei, H.C.; Harmsen, M.C.; van Kooten, T.G.; Sharma, P.K. Viscoelastic Properties of Plasma-Agarose Hydrogels Dictate Favorable Fibroblast Responses for Skin Tissue Engineering Applications. *Biomater. Adv.* **2022**, *139*, 212967. [CrossRef]
85. Sattari, S.; Dadkhah Tehrani, A.; Adeli, M. PH-Responsive Hybrid Hydrogels as Antibacterial and Drug Delivery Systems. *Polymers* **2018**, *10*, 660. [CrossRef]
86. Vilela, P.B.; Dalalibera, A.; Becegato, V.A.; Paulino, A.T. Single-Component and Multi-Component Metal Abatement in Water Using a Hydrogel Based on Chitosan: Characterization, Isotherm, Kinetic, and Thermodynamic Results. *Water Air Soil Pollut.* **2020**, *231*, 507. [CrossRef]
87. Guven, M.N.; Seckin Altuncu, M.; Demir Duman, F.; Eren, T.N.; Yagci Acar, H.; Avci, D. Bisphosphonate-Functionalized Poly(β-Amino Ester) Network Polymers. *J. Biomed. Mater. Res.* **2017**, *105*, 1412–1421. [CrossRef]
88. Ha, J.H.; Lim, J.H.; Kim, J.W.; Cho, H.-Y.; Jo, S.G.; Lee, S.H.; Eom, J.Y.; Lee, J.M.; Chung, B.G. Conductive GelMA–Collagen–AgNW Blended Hydrogel for Smart Actuator. *Polymers* **2021**, *13*, 1217. [CrossRef]
89. Scimeca, M.; Bischetti, S.; Lamsira, H.K.; Bonfiglio, R.; Bonanno, E. Energy Dispersive X-Ray (EDX) Microanalysis: A Powerful Tool in Biomedical Research and Diagnosis. *Eur. J. Histochem.* **2018**, *62*, 2841. [CrossRef]
90. Nichol, J.W.; Koshy, S.T.; Bae, H.; Hwang, C.M.; Yamanlar, S.; Khademhosseini, A. Cell-Laden Microengineered Gelatin Methacrylate Hydrogels. *Biomaterials* **2010**, *31*, 5536–5544. [CrossRef]
91. Martinez-Garcia, F.D.; Valk, M.M.; Sharma, P.K.; Burgess, J.K.; Harmsen, M.C. Adipose Tissue-Derived Stromal Cells Alter the Mechanical Stability and Viscoelastic Properties of Gelatine Methacryloyl Hydrogels. *IJMS* **2021**, *22*, 10153. [CrossRef]

92. Chimenti, I.; Rizzitelli, G.; Gaetani, R.; Angelini, F.; Ionta, V.; Forte, E.; Frati, G.; Schussler, O.; Barbetta, A.; Messina, E.; et al. Human Cardiosphere-Seeded Gelatin and Collagen Scaffolds as Cardiogenic Engineered Bioconstructs. *Biomaterials* **2011**, *32*, 9271–9281. [CrossRef]
93. McKinlay, K.J.; Allison, F.J.; Scotchford, C.A.; Grant, D.M.; Oliver, J.M.; King, J.R.; Wood, J.V.; Brown, P.D. Comparison of Environmental Scanning Electron Microscopy with High Vacuum Scanning Electron Microscopy as Applied to the Assessment of Cell Morphology. *J. Biomed. Mater. Res.* **2004**, *69*, 359–366. [CrossRef]
94. Bokstad, M.; Medalia, O. Correlative Light Electron Microscopy as a Navigating Tool for Cryo-Electron Tomography Analysis. In *Fluorescence Microscopy*; Elsevier: Amsterdam, The Netherlands, 2014; pp. 121–131, ISBN 978-0-12-409513-7.
95. Aston, R.; Sewell, K.; Klein, T.; Lawrie, G.; Grøndahl, L. Evaluation of the Impact of Freezing Preparation Techniques on the Characterisation of Alginate Hydrogels by Cryo-SEM. *Eur. Polym. J.* **2016**, *82*, 1–15. [CrossRef]
96. Kuleshova, L.L.; Gouk, S.S.; Hutmacher, D.W. Vitrification as a Prospect for Cryopreservation of Tissue-Engineered Constructs. *Biomaterials* **2007**, *28*, 1585–1596. [CrossRef]
97. Tavukcuoglu, S.; Al-Azawi, T.; Khaki, A.A.; Al-Hasani, S. Is Vitrification Standard Method of Cryopreservation. *Middle East Fertil. Soc. J.* **2012**, *17*, 152–156. [CrossRef]
98. Ivan'kova, E.M.; Dobrovolskaya, I.P.; Popryadukhin, P.V.; Kryukov, A.; Yudin, V.E.; Morganti, P. In-Situ Cryo-SEM Investigation of Porous Structure Formation of Chitosan Sponges. *Polym. Test.* **2016**, *52*, 41–45. [CrossRef]
99. Ji, C.; Annabi, N.; Khademhosseini, A.; Dehghani, F. Fabrication of Porous Chitosan Scaffolds for Soft Tissue Engineering Using Dense Gas CO2. *Acta Biomater.* **2011**, *7*, 1653–1664. [CrossRef]
100. Schnabel-Lubovsky, M.; Kossover, O.; Melino, S.; Nanni, F.; Talmon, Y.; Seliktar, D. Visualizing Cell-laden Fibrin-based Hydrogels Using Cryogenic Scanning Electron Microscopy and Confocal Microscopy. *J. Tissue Eng. Regen. Med.* **2019**, *13*, 587–598. [CrossRef]
101. Valot, L.; Maumus, M.; Brunel, L.; Martinez, J.; Amblard, M.; Noël, D.; Mehdi, A.; Subra, G. A Collagen-Mimetic Organic-Indorganic Hydrogel for Cartilage Engineering. *Gels* **2021**, *7*, 73. [CrossRef]
102. Pan, T.; Song, W.; Cao, X.; Wang, Y. 3D Bioplotting of Gelatin/Alginate Scaffolds for Tissue Engineering: Influence of Crosslinking Degree and Pore Architecture on Physicochemical Properties. *J. Mater. Sci. Technol.* **2016**, *32*, 889–900. [CrossRef]
103. Stabentheiner, E.; Zankel, A.; Pölt, P. Environmental Scanning Electron Microscopy (ESEM)—A Versatile Tool in Studying Plants. *Protoplasma* **2010**, *246*, 89–99. [CrossRef]
104. Kaberova, Z.; Karpushkin, E.; Nevoralová, M.; Vetrík, M.; Šlouf, M.; Dušková-Smrčková, M. Microscopic Structure of Swollen Hydrogels by Scanning Electron and Light Microscopies: Artifacts and Reality. *Polymers* **2020**, *12*, 578. [CrossRef] [PubMed]
105. Spiller, K.L.; Holloway, J.L.; Gribb, M.E.; Lowman, A.M. Design of Semi-Degradable Hydrogels Based on Poly(Vinyl Alcohol) and Poly(Lactic-Co-Glycolic Acid) for Cartilage Tissue Engineering. *J. Tissue Eng. Regen. Med.* **2011**, *5*, 636–647. [CrossRef] [PubMed]
106. Peers, S.; Alcouffe, P.; Montembault, A.; Ladavière, C. Embedment of Liposomes into Chitosan Physical Hydrogel for the Delayed Release of Antibiotics or Anaesthetics, and Its First ESEM Characterization. *Carbohydr. Polym.* **2020**, *229*, 229–115532. [CrossRef]
107. Rizzi, S.C.; Heath, D.J.; Coombes, A.G.A.; Bock, N.; Textor, M.; Downes, S. Biodegradable Polymer/Hydroxyapatite Composites: Surface Analysis and Initial Attachment of Human Osteoblasts. *J. Biomed. Mater. Res.* **2001**, *55*, 475–486. [CrossRef]
108. Van Vlierberghe, S.; Dubruel, P.; Lippens, E.; Masschaele, B.; van Hoorebeke, L.; Cornelissen, M.; Unger, R.; Kirkpatrick, C.J.; Schacht, E. Toward Modulating the Architecture of Hydrogel Scaffolds: Curtains versus Channels. *J. Mater. Sci. Mater. Med.* **2008**, *19*, 1459–1466. [CrossRef]
109. Boerckel, J.D.; Mason, D.E.; McDermott, A.M.; Alsberg, E. Microcomputed Tomography: Approaches and Applications in Bioengineering. *Stem Cell Res. Ther.* **2014**, *5*, 144. [CrossRef]
110. Morelhão, S.L. Fundamentals of X-Ray Physics. In *Computer Simulation Tools for X-ray Analysis*; Graduate Texts in Physics; Springer International Publishing: Cham, Switzerland, 2016; pp. 1–57, ISBN 978-3-319-19553-7.
111. Olăreț, E.; Stancu, I.-C.; Iovu, H.; Serafim, A. Computed Tomography as a Characterization Tool for Engineered Scaffolds with Biomedical Applications. *Materials* **2021**, *14*, 6763. [CrossRef] [PubMed]
112. Bouxsein, M.L.; Boyd, S.K.; Christiansen, B.A.; Guldberg, R.E.; Jepsen, K.J.; Müller, R. Guidelines for Assessment of Bone Microstructure in Rodents Using Micro-Computed Tomography. *J. Bone Miner. Res.* **2010**, *25*, 1468–1486. [CrossRef] [PubMed]
113. Wu, Y.; Adeeb, S.; Doschak, M.R. Using Micro-CT Derived Bone Microarchitecture to Analyze Bone Stiffness Â€“ A Case Study on Osteoporosis Rat Bone. *Front. Endocrinol.* **2015**, *6*, 80. [CrossRef] [PubMed]
114. Hua, Y.; Bi, R.; Zhang, Y.; Xu, L.; Guo, J.; Li, Y. Different Bone Sites-Specific Response to Diabetes Rat Models: Bone Density, Histology and Microarchitecture. *PLoS ONE* **2018**, *13*, e0205503. [CrossRef] [PubMed]
115. Feldkamp, L.A.; Goldstein, S.A.; Parfitt, M.A.; Jesion, G.; Kleerekoper, M. The Direct Examination of Three-Dimensional Bone Architecture in Vitro by Computed Tomography. *J. Bone Miner. Res.* **2009**, *4*, 3–11. [CrossRef] [PubMed]
116. Chatterjee, K.; Lin-Gibson, S.; Wallace, W.E.; Parekh, S.H.; Lee, Y.J.; Cicerone, M.T.; Young, M.F.; Simon, C.G. The Effect of 3D Hydrogel Scaffold Modulus on Osteoblast Differentiation and Mineralization Revealed by Combinatorial Screening. *Biomaterials* **2010**, *31*, 5051–5062. [CrossRef]
117. Guda, T.; Oh, S.; Appleford, M.R.; Ong, J.L. Bilayer Hydroxyapatite Scaffolds for Maxillofacial Bone Tissue Engineering. *Int. J. Oral Maxillofac. Implants* **2012**, *27*, 288–294.
118. Gothard, D.; Smith, E.L.; Kanczler, J.M.; Black, C.R.; Wells, J.A.; Roberts, C.A.; White, L.J.; Qutachi, O.; Peto, H.; Rashidi, H.; et al. In Vivo Assessment of Bone Regeneration in Alginate/Bone ECM Hydrogels with Incorporated Skeletal Stem Cells and Single Growth Factors. *PLoS ONE* **2015**, *10*, e0145080. [CrossRef]

119. Celikkin, N.; Mastrogiacomo, S.; Walboomers, X.; Swieszkowski, W. Enhancing X-Ray Attenuation of 3D Printed Gelatin Methacrylate (GelMA) Hydrogels Utilizing Gold Nanoparticles for Bone Tissue Engineering Applications. *Polymers* **2019**, *11*, 367. [CrossRef]
120. Behravesh, E.E.; Timmer, M.D.; Lemoine, J.J.; Liebschner, M.A.K.; Mikos, A.G. Evaluation of the in Vitro Degradation of Macroporous Hydrogels Using Gravimetry, Confined Compression Testing, and Microcomputed Tomography. *Biomacromolecules* **2002**, *3*, 1263–1270. [CrossRef]
121. Hedberg, E.L.; Shih, C.K.; Lemoine, J.J.; Timmer, M.D.; Liebschner, M.A.; Jansen, J.A.; Mikos, A.G. In Vitro Degradation of Porous Poly(Propylene Fumarate)/Poly(Dl-Lactic-Co-Glycolic Acid) Composite Scaffolds. *Biomaterials* **2005**, *26*, 3215–3225. [CrossRef]
122. Shi, M.; Kretlow, J.D.; Nguyen, A.; Young, S.; Scott Baggett, L.; Wong, M.E.; Kurtis Kasper, F.; Mikos, A.G. Antibiotic-Releasing Porous Polymethylmethacrylate Constructs for Osseous Space Maintenance and Infection Control. *Biomaterials* **2010**, *31*, 4146–4156. [CrossRef]
123. Vásárhelyi, L.; Kónya, Z.; Kukovecz, Á.; Vajtai, R. Microcomputed Tomography–Based Characterization of Advanced Materials: A Review. *Mater. Today Adv.* **2020**, *8*, 100084. [CrossRef]
124. Dubruel, P.; Unger, R.; van Vlierberghe, S.; Cnudde, V.; Jacobs, P.J.S.; Schacht, E.; Kirkpatrick, C.J. Porous Gelatin Hydrogels: 2. In Vitro Cell Interaction Study. *Biomacromolecules* **2007**, *8*, 338–344. [CrossRef] [PubMed]
125. Offeddu, G.S.; Ashworth, J.C.; Cameron, R.E.; Oyen, M.L. Structural Determinants of Hydration, Mechanics and Fluid Flow in Freeze-Dried Collagen Scaffolds. *Acta Biomater.* **2016**, *41*, 193–203. [CrossRef] [PubMed]
126. Wu, X.; Wang, X.; Chen, X.; Yang, X.; Ma, Q.; Xu, G.; Yu, L.; Ding, J. Injectable and Thermosensitive Hydrogels Mediating a Universal Macromolecular Contrast Agent with Radiopacity for Noninvasive Imaging of Deep Tissues. *Bioact. Mater.* **2021**, *6*, 4717–4728. [CrossRef]
127. Patrick, P.S.; Bear, J.C.; Fitzke, H.E.; Zaw-Thin, M.; Parkin, I.P.; Lythgoe, M.F.; Kalber, T.L.; Stuckey, D.J. Radio-Metal Cross-Linking of Alginate Hydrogels for Non-Invasive in Vivo Imaging. *Biomaterials* **2020**, *243*, 119930. [CrossRef]
128. Faraj, K.A.; Cuijpers, V.M.J.I.; Wismans, R.G.; Walboomers, X.F.; Jansen, J.A.; van Kuppevelt, T.H.; Daamen, W.F. Micro-Computed Tomographical Imaging of Soft Biological Materials Using Contrast Techniques. *Tissue Eng. Part C Methods* **2009**, *15*, 493–499. [CrossRef]
129. Lichtman, J.W.; Conchello, J.-A. Fluorescence Microscopy. *Nat. Methods* **2005**, *2*, 910–919. [CrossRef]
130. Hickey, S.M.; Ung, B.; Bader, C.; Brooks, R.; Lazniewska, J.; Johnson, I.R.D.; Sorvina, A.; Logan, J.; Martini, C.; Moore, C.R.; et al. Fluorescence Microscopy—An Outline of Hardware, Biological Handling, and Fluorophore Considerations. *Cells* **2021**, *11*, 35. [CrossRef]
131. Rai, V.; Dey, N. The Basics of Confocal Microscopy. In *Laser Scanning, Theory and Applications*; Wang, C.-C., Ed.; InTech: London, UK, 2011; ISBN 978-953-307-205-0.
132. Moshkov, A. Confocal Laser Scanning Microscopy of Living Cells. In *Fluorescence Methods for Investigation of Living Cells and Microorganisms*; Grigoryeva, N., Ed.; IntechOpen: London, UK, 2020; ISBN 978-1-83968-039-7.
133. Bagnaninchi, P.O.; Yang, Y.; Zghoul, N.; Maffulli, N.; Wang, R.K.; El Haj, A.J. Chitosan Microchannel Scaffolds for Tendon Tissue Engineering Characterized Using Optical Coherence Tomography. *Tissue Eng.* **2007**, *13*, 323–331. [CrossRef]
134. Bancelin, S.; Aimé, C.; Gusachenko, I.; Kowalczuk, L.; Latour, G.; Coradin, T.; Schanne-Klein, M.-C. Determination of Collagen Fibril Size via Absolute Measurements of Second-Harmonic Generation Signals. *Nat. Commun.* **2014**, *5*, 4920. [CrossRef]
135. Hwang, Y.J.; Lyubovitsky, J.G. Collagen Hydrogel Characterization: Multi-Scale and Multi-Modality Approach. *Anal. Methods* **2011**, *3*, 529–536. [CrossRef] [PubMed]
136. Zipfel, W.R.; Williams, R.M.; Webb, W.W. Nonlinear Magic: Multiphoton Microscopy in the Biosciences. *Nat. Biotechnol.* **2003**, *21*, 1369–1377. [CrossRef] [PubMed]
137. Zipfel, W.R.; Williams, R.M.; Christie, R.; Nikitin, A.Y.; Hyman, B.T.; Webb, W.W. Live Tissue Intrinsic Emission Microscopy Using Multiphoton-Excited Native Fluorescence and Second Harmonic Generation. *Proc. Natl. Acad. Sci. USA* **2003**, *100*, 7075–7080. [CrossRef] [PubMed]
138. Raub, C.B.; Suresh, V.; Krasieva, T.; Lyubovitsky, J.; Mih, J.D.; Putnam, A.J.; Tromberg, B.J.; George, S.C. Noninvasive Assessment of Collagen Gel Microstructure and Mechanics Using Multiphoton Microscopy. *Biophys. J.* **2007**, *92*, 2212–2222. [CrossRef]
139. Theodossiou, T.; Rapti, G.S.; Hovhannisyan, V.; Georgiou, E.; Politopoulos, K.; Yova, D. Thermally Induced Irreversible Conformational Changes in Collagen Probed by Optical Second Harmonic Generation and Laser-Induced Fluorescence. *Lasers Med. Sci.* **2002**, *17*, 34–41. [CrossRef]
140. Williams, R.M.; Zipfel, W.R.; Webb, W.W. Interpreting Second-Harmonic Generation Images of Collagen I Fibrils. *Biophys. J.* **2005**, *88*, 1377–1386. [CrossRef]
141. Raub, C.B.; Unruh, J.; Suresh, V.; Krasieva, T.; Lindmo, T.; Gratton, E.; Tromberg, B.J.; George, S.C. Image Correlation Spectroscopy of Multiphoton Images Correlates with Collagen Mechanical Properties. *Biophys. J.* **2008**, *94*, 2361–2373. [CrossRef]
142. *Second Harmonic Generation Imaging*; Pavone, P.S. (Ed.) Series in cellular and clinical imaging; CRC Press: Boca Raton, FL, USA, 2014; ISBN 978-1-4398-4915-6.
143. Tjin, G.; Xu, P.; Kable, S.H.; Kable, E.P.; Burgess, J.K. Quantification of Collagen I in Airway Tissues Using Second Harmonic Generation. *J. Biomed. Opt.* **2014**, *19*, 36005. [CrossRef]
144. Cox, G.; Kable, E.; Jones, A.; Fraser, I.; Manconi, F.; Gorrell, M.D. 3-Dimensional Imaging of Collagen Using Second Harmonic Generation. *J. Struct. Biol.* **2003**, *141*, 53–62. [CrossRef]

145. Zoumi, A.; Yeh, A.; Tromberg, B.J. Imaging Cells and Extracellular Matrix in Vivo by Using Second-Harmonic Generation and Two-Photon Excited Fluorescence. *Proc. Natl. Acad. Sci. USA* **2002**, *99*, 11014–11019. [CrossRef]
146. Sanen, K.; Paesen, R.; Luyck, S.; Phillips, J.; Lambrichts, I.; Martens, W.; Ameloot, M. Label-Free Mapping of Microstructural Organisation in Self-Aligning Cellular Collagen Hydrogels Using Image Correlation Spectroscopy. *Acta Biomater.* **2016**, *30*, 258–264. [CrossRef] [PubMed]
147. Raub, C.B.; Putnam, A.J.; Tromberg, B.J.; George, S.C. Predicting Bulk Mechanical Properties of Cellularized Collagen Gels Using Multiphoton Microscopy. *Acta Biomater.* **2010**, *6*, 4657–4665. [CrossRef]
148. Tjin, G.; White, E.S.; Faiz, A.; Sicard, D.; Tschumperlin, D.J.; Mahar, A.; Kable, E.P.W.; Burgess, J.K. Lysyl Oxidases Regulate Fibrillar Collagen Remodelling in Idiopathic Pulmonary Fibrosis. *Dis. Model Mech.* **2017**, *10*, 1301–1312. [CrossRef] [PubMed]
149. Boddupalli, A.; Bratlie, K.M. Second Harmonic Generation Microscopy of Collagen Organization in Tunable, Environmentally Responsive Alginate Hydrogels. *Biomater. Sci.* **2019**, *7*, 1188–1199. [CrossRef] [PubMed]
150. Binnig, G.; Quate, C.F.; Gerber, C. Atomic Force Microscope. *Phys. Rev. Lett.* **1986**, *56*, 930–933. [CrossRef]
151. Radmacher, M.; Tillamnn, R.; Fritz, M.; Gaub, H. From Molecules to Cells: Imaging Soft Samples with the Atomic Force Microscope. *Science* **1992**, *257*, 1900–1905. [CrossRef]
152. Cappella, B.; Dietler, G. Force-Distance Curves by Atomic Force Microscopy. *Surf. Sci. Rep.* **1999**, *34*, 1–104. [CrossRef]
153. Alessandrini, A.; Facci, P. AFM: A Versatile Tool in Biophysics. *Meas. Sci. Technol.* **2005**, *16*, R65–R92. [CrossRef]
154. Edmondson, R.; Broglie, J.J.; Adcock, A.F.; Yang, L. Three-Dimensional Cell Culture Systems and Their Applications in Drug Discovery and Cell-Based Biosensors. *ASSAY Drug Dev. Technol.* **2014**, *12*, 207–218. [CrossRef]
155. Jensen, C.; Teng, Y. Is It Time to Start Transitioning From 2D to 3D Cell Culture? *Front. Mol. Biosci.* **2020**, *7*, 33. [CrossRef]
156. Román, J.; Cabañas, M.V.; Peña, J.; Vallet-Regí, M. Control of the Pore Architecture in Three-Dimensional Hydroxyapatite-Reinforced Hydrogel Scaffolds. *Sci. Technol. Adv. Mater.* **2011**, *12*, 045003. [CrossRef] [PubMed]
157. Studenovská, H.; Šlouf, M.; Rypáček, F. Poly(HEMA) Hydrogels with Controlled Pore Architecture for Tissue Regeneration Applications. *J. Mater. Sci. Mater. Med.* **2008**, *19*, 615–621. [CrossRef] [PubMed]
158. Siemsen, K.; Rajput, S.; Rasch, F.; Taheri, F.; Adelung, R.; Lammerding, J.; Selhuber-Unkel, C. Tunable 3D Hydrogel Microchannel Networks to Study Confined Mammalian Cell Migration. *Adv. Healthcare Mater.* **2021**, *10*, 2100625. [CrossRef]
159. Ford, M.C.; Bertram, J.P.; Hynes, S.R.; Michaud, M.; Li, Q.; Young, M.; Segal, S.S.; Madri, J.A.; Lavik, E.B. A Macroporous Hydrogel for the Coculture of Neural Progenitor and Endothelial Cells to Form Functional Vascular Networks. *Proc. Natl. Acad. Sci. USA* **2006**, *103*, 2512–2517. [CrossRef] [PubMed]
160. Nazarov, R.; Jin, H.-J.; Kaplan, D.L. Porous 3-D Scaffolds from Regenerated Silk Fibroin. *Biomacromolecules* **2004**, *5*, 718–726. [CrossRef]
161. Vo, J.; Mastoor, Y.; Mathieu, P.S.; Clyne, A.M. A Simple Method to Align Cells on 3D Hydrogels Using 3D Printed Molds. *Biomed. Eng. Adv.* **2021**, *1*, 100001. [CrossRef]
162. Vignaud, T.; Ennomani, H.; Théry, M. Polyacrylamide Hydrogel Micropatterning. In *Methods in Cell Biology*; Elsevier: Amsterdam, The Netherlands, 2014; Volume 120, pp. 93–116, ISBN 978-0-12-417136-7.
163. Yeh, J.; Ling, Y.; Karp, J.M.; Gantz, J.; Chandawarkar, A.; Eng, G.; Blumling III, J.; Langer, R.; Khademhosseini, A. Micromolding of Shape-Controlled, Harvestable Cell-Laden Hydrogels. *Biomaterials* **2006**, *27*, 5391–5398. [CrossRef]
164. Lu, D.; Zeng, Z.; Geng, Z.; Guo, C.; Pei, D.; Zhang, J.; Yu, S. Macroporous Methacrylated Hyaluronic Acid Hydrogel with Different Pore Sizes for in Vitro and in Vivo Evaluation of Vascularization. *Biomed. Mater.* **2022**, *17*, 025006. [CrossRef]
165. Chiu, Y.-C.; Cheng, M.-H.; Engel, H.; Kao, S.-W.; Larson, J.C.; Gupta, S.; Brey, E.M. The Role of Pore Size on Vascularization and Tissue Remodeling in PEG Hydrogels. *Biomaterials* **2011**, *32*, 6045–6051. [CrossRef]
166. Kim, H.D.; Valentini, R.F. Retention and Activity of BMP-2 in Hyaluronic Acid-Based Scaffolds in Vitro. *J. Biomed. Mater. Res.* **2002**, *59*, 573–584. [CrossRef]
167. Kim, H.J.; Kim, U.-J.; Vunjak-Novakovic, G.; Min, B.-H.; Kaplan, D.L. Influence of Macroporous Protein Scaffolds on Bone Tissue Engineering from Bone Marrow Stem Cells. *Biomaterials* **2005**, *26*, 4442–4452. [CrossRef] [PubMed]
168. Grove, C.; Jerram, D.A. JPOR: An ImageJ Macro to Quantify Total Optical Porosity from Blue-Stained Thin Sections. *Comput. Geosci.* **2011**, *37*, 1850–1859. [CrossRef]
169. Haeri, M.; Haeri, M. ImageJ Plugin for Analysis of Porous Scaffolds Used in Tissue Engineering. *J. Open Res. Softw.* **2015**, *3*. [CrossRef]
170. Dušková-Smrčková, M.; Zavřel, J.; Bartoš, M.; Kaberova, Z.; Filová, E.; Zárubová, J.; Šlouf, M.; Michálek, J.; Vampola, T.; Kubies, D. Communicating Macropores in PHEMA-Based Hydrogels for Cell Seeding: Probabilistic Open Pore Simulation and Direct Micro-CT Proof. *Mater. Des.* **2021**, *198*, 109312. [CrossRef]
171. Cengiz, I.F.; Oliveira, J.M.; Reis, R.L. Micro-CT—A Digital 3D Microstructural Voyage into Scaffolds: A Systematic Review of the Reported Methods and Results. *Biomater. Res.* **2018**, *22*, 26. [CrossRef]